Arabian Journal of Chemistry (2023) **16**, 105099

King Saud University

Arabian Journal of Chemistry

www.ksu.edu.sa
www.sciencedirect.com

ORIGINAL ARTICLE

Synthesis, microstructure, magnetic and electromagnetic behavior of graphene oxide/hexagonal barium ferrite aerogel nanocomposites within the frequency range of 1–18 GHz

Reza Ghorbanpour Ghartavool [a], Gholam Reza Gordani [a], Mohammad Reza Loghman Estarki [a], Majid Tavoosi [a], Mehdi Mazaheri Forushani [a], Esmail Kiani [b]

[a] *Department of Materials Engineering, Malek Ashtar University Of Technology, Iran*
[b] *Department of Electroceram and Electrical Engineering, Malek Ashtar University of Technology, Iran*

Received 10 March 2023; accepted 19 June 2023
Available online 26 June 2023

KEYWORDS

Dielectric loss;
Dipole polarization;
EM wave absorbent;
Nanocomposite;
Graphene oxide;
Aerogel;
Thickness effect;
Loading ratio

Abstract The fabrication of lightweight graphene oxide aerogel (GOA) composites with barium ferrite (BF) nanoparticles is investigated in this study as a method of shielding electronic and telecommunication equipment from electromagnetic radiation. The effects of various weight percentages of barium ferrite nanoparticles on the microstructure, phase, magnetic characteristics, and wave absorption were investigated. The XRD, FTIR, Raman spectroscopy, X-ray Photoelectron spectroscopy (XPS), thermal gravimetric analysis (TGA) and differential scanning calorimetry (DSC), FESEM, and vibrational magnetometry (VSM) and the vector network analyzer (VNA) were used to characterize the sample.

Results show that barium ferrite nanoparticles had a saturation magnetization of 42.94 emu/g, whereas graphene oxide aerogel composite containing 67 wt% of barium ferrite nanoparticles had a saturation magnetization of 29 emu/g. The Coercivity of the composite rose when the amount of barium ferrite nanoparticles was reduced. Within the matched frequency of 12.1 GHz and an effective absorption bandwidth (RL < -10 dB) of 2.6 GHz, the graphene aerogel nanocomposite

E-mail addresses: gordani@gmail.com (G.R. Gordani), Mrlestarki@mut-es.ac.ir (M.R. Loghman Estarki)
Peer review under responsibility of King Saud University.

Production and hosting by Elsevier

https://doi.org/10.1016/j.arabjc.2023.105099

sample with a thickness of 4 mm and 40 wt% of barium ferrite nanoparticles had the highest level of reflection loss (−43 dB).

1. Introduction

Electromagnetic pollution is progressively created by industrial and electronic equipment, seriously threatening human health (Zhou et al., 2019). This issue has led to the rapid development of electromagnetic wave-absorbent materials (Liu et al., 2023). Over the past decades, ferrite materials, conductive polymers, composite materials, magnetic metal powders, and ceramics have been examined. These materials have limited applications due to large density, heavyweight, and environmental degradation in aerospace as well as electronic and communication technologies. High protectivity within a wide frequency range, small thickness, and lightweight concurrently are the necessities for these materials (Shen et al., 2019; Xu et al., 2021; Zhu et al., 2023; Magisetty et al., 2018; Majcher et al., 2020; Cheng et al., 2020).

Graphene materials, as a very lightweight and low-density material, have a two-dimensional structure and have been of interest to researchers as part of absorbent materials for electromagnetic (EM) wave absorption (Sun et al., 2020; Xia et al., 2022).

In all cases, special methods should be designed to fully exploit graphene properties to convert two-dimensional materials to three-dimensional structures. Thus, the preparation and characterization of graphene materials with a three-dimensional structure, such as aerogels, hydrogels, and thick films are very important (Zhang et al., 2016; Yi et al., 2020; Jia et al., 2021). Among these structures, aerogels have great potential and have been extensively examined. It suffices to state that these materials show higher electric conductivity, which has been prepared through the dispersion of graphene sheets (Shen et al., 2019; Sun et al., 2020).

Graphene aerogel (GA) is a low-density and porous material composed of a lattice of graphene-compressed sheets. By blending and mixing magnetic particles and dielectric materials, the aerogel of graphene composites can be synthesized, which is very effective in electromagnetic wave absorption properties (Huang et al., 2021). Zhao et al. prepared a three-dimensional ACNT/BF/rGO aerogel composite consisting of reduced graphene oxide (rGO), amorphous carbon nanotubes (ACNT), and barium ferrite (BF) nanoparticles through a self-propagating combustion process for electromagnetic wave absorption in the frequency range of 2 to 18 GHz. ACNT and rGO were used to enhance conductivity and dielectric losses, while barium ferrite nanoparticles were incorporated to improve magnetic losses. The ACNT/rGO/BF composite exhibited a reflection loss of −19.03 dB at 11.04 GHz, and the frequency bandwidth was 3.8 GHz at −10 dB (Zhao et al., 2017).

Zhang and coworkers (Zhang et al., 2018) synthesized reduced graphene oxide/ polypyrrole nanotubes/Fe_3O_4 aerogel (GPFA) nanocomposite for exploring the protective features against electromagnetic waves via the hydrothermal method. The maximum rGA reflection loss (RL) was −37.8 dB at 7.8 GHz with a thickness of 4.5 mm; the maximum reflection loss of GFA was −47.1 dB at 8.15 GHz with a thickness of 4.5 mm; and the maximum RL value of GPFA was −49.2 dB at 11.8 GHz with a thickness of 3 mm. The bandwidth of reflection loss of the GA, GFA, and GPFA was 3.7, 4.3, and 6.1 GHz within frequency ranges of 6.2–9.9, 6.65–10.95, and 9.8–15.9 GHz, respectively. It was found that upon adding Fe_3O_4 nanoparticles and PP_y nanotubes, the absorption properties of the EM wave increased in the RGO aerogel (Zhang et al., 2018).

Gupta et al. (Gupta et al., 2019) synthesized 3D graphene oxide aerogels composed of cobalt ferrite (CFO) nanoparticles and zinc oxide nanorods. The G-01 (GO/1%CFO) aerogel reflection loss increased from −2.56 to −4.22 dB, while the RL value also rose from 25.07 dB to 28.10 dB in (GO/1%CFO/1%ZnO aerogel), indicating the essential role of ZnO nanorods. With the increase in the reflection loss due to the mixing of nonconductive CFO nanoparticles and ZnO nanoparticles, impedance matching was increased. Better protection of EMI waves with dielectric losses is due to ZnO nanoparticles, and the magnetic losses are due to the presence of CFO nanoparticles. Overall, due to low density, high porosity, and wide area, graphene aerogel showed a total EMI protective effect of 25.07 dB at a thickness of 5 mm, which would grow to 42.10 dB upon adding cobalt ferrite nanoparticles. They indicated the addition of magnetic cobalt ferrite not only contributed to increasing total protection against EMI in aerogels but also led to an improvement in EM wave absorption from 37.738% to 87.788%. With a further combination of ZnO nanorods alongside cobalt ferrite nanoparticles in aerogels, the total EMI protective effect and EM wave absorption increased to 38.56 dB and 93.655%, respectively (Gupta et al., 2019).

Feng et al. (2016) demonstrated that the CoNi/nitrogen-doped graphene hybrids, utilizing the optimized combination of magnetic properties of CoNi nanoparticles and electrical properties of nitrogen-doped graphene, exhibit a maximum RL value of −22 dB at 10 GHz with a thickness of only 2.0 mm. The effective absorption bandwidth, with a reflection loss below −10 dB, ranges from 3.6 GHz to 18 GHz for thicknesses of 1.35 mm to 5.0 mm.

Ding et al. (2016) synthesized a 3D $CoFe_2O_4$ / N-doped reduced graphene oxide (CNGA) aerogel composite via solvothermal and lyophilization methods. The CNGA sample showed the best microwave absorption performance, with a fine thickness of 2.1 mm. The CNGA showed a minimum reflection loss of −60.42 dB and maximum effective absorption bandwidth of 6.48 GHz within 11.44 – 17.92 GHz. In this composite, the minimum reflection loss was –32.36 dB at a thickness of 2.2 mm, covering the X band at 3 mm. Ding et al. (Wang et al., 2013) synthesized reduced graphene oxide (RGO) nanocomposites with embedded Fe_3O_4/Fe nanoparticles (FeNR@rGO) via the hydrothermal method for investigating the electromagnetic wave absorption properties. This nanocomposite sample (thickness = 4.0 mm) exhibited a minimum RL value of –23.09 dB at 9.16 GHz.

Wang and his colleagues (Wang et al., 2013) synthesized a type of nanocomposite for electromagnetic wave absorption in the frequency range of 2 to 18 GHz using graphene nanosheets (GNS) and $Ni_{0.8}Zn_{0.2}Ce_{0.06}Fe_{1.94}O_4$ nanoparticles via a deoxidation technique method. The $Ni_{0.8}Zn_{0.2}Ce_{0.06}Fe_{1.94}O_4$/GNS nanocomposite exhibited a minimum RL value of −37.4 dB at 12.3 GHz. Additionally, it displayed a broad peak with a bandwidth below −10 dB, ranging from 10.7 to 15.2 GHz.

Ferrites nanoparticles as an EM wave absorbent have been studied extensively. Barium ferrite is used in electromagnetic wave absorbent materials due to high magnetic permittivity. Also, high Curie temperature, good chemical stability, and good corrosion resistance are among the advantages of barium ferrite (Mathews and Rajan Babu, 2021). To the best of our knowledge, there is no report on the effect of hexagonal barium ferrite nanoparticle content on the EM wave behavior of GO-barium ferrite aerogel composites. Furthermore, the majority of reports obtained good reflection loss with three components and high density (Huang et al., 2021; Zhao et al., 2017; Zhang et al., 2018; Gupta et al., 2019; Feng et al., 2016; Wang et al., 2020; Ding et al., 2016; Wang et al., 2013), however, in this works lightweight EM wave absorbent was prepared with two parts of GO nanosheets and BF nanoparticles.

Table 1 The materials used in the synthesis of samples.

Material name	Chemical formula	Company
Iron chloride	$FeCl_3{\cdot}6H_2O$	Merck
Barium chloride	$BaCl_2{\cdot}2H_2O$	Merck
Sodium hydroxide	NaOH	Merck
Graphene oxide	GO	Merck

In this research, a graphene aerogel structure containing ferrite nanoparticles is used, so that through the good dielectric loss properties of graphene aerogel, the magnetic losses of ferrite nanoparticles would cause attenuation of electromagnetic waves inside the final product. It is expected that the 3D and porous structure of this product would cause a synergistic effect on the absorption mechanism and enhance the electromagnetic wave absorption properties of the composite materials compared to conventional materials.

2. Experimental

2.1. Materials

The raw materials used in this research are outlined in Table 1. The materials have been used without purification.

2.2. Synthesis of graphene aerogel/barium ferrite nanoparticle composites

For synthesizing the nanocomposite, 0.25 g graphene oxide was added to 70 ml deionized water and homogenized via ultrasound device (Toposonic model, Iran) for 30 min. Next, 0.8 g of barium ferrite nanoparticles was added to the mixture and ultrasonicated for 30 min. The mixture was immediately transferred into the Teflon-lined autoclave, and the autoclave was placed in the oven at 150 °C for 5 h. Once the autoclave cooled down to room temperature, the graphene hydrogel/barium ferrite nanoparticles were placed inside a freeze drier(Dena Company, Iran) for 24 h. Fig. 1 shows a schematic of the synthesis steps of graphene oxide aerogel nanocomposites with the addition of barium ferrite nanoparticles.

For the synthesis of 3D nanocomposite samples, the amount of graphene oxide was kept constant, while the amount of barium ferrite nanoparticles was changed at 0.125 g, 0.166 g, 0.375 g, and 0.5 g. The aim was to investigate the effect of different weight percentages of barium ferrite nanoparticles on graphene oxide sheets on the EM wave absorption. The samples are named according to Table 2.

2.3. Test methods

For phase characterization of the composites, in this research, an XRD device (ASENWARE, AW-XDM300) (Sadeghi et al., 2022; Sivaraman et al., 2022; Jalil et al., 2021; Radjehi et al., 2023; Ghasemvand et al., 2023) was used with an X-ray wavelength of CuK_α = 0.15140 nm.

To detect functional groups in the synthesized nanoparticles, an FTIR device (Infralum ft-08, LUMEX Co., Russia) (Suanto et al., 2022) was used within the wavenumber of 400–4000 cm^{-1}. The bulk density of the sample was measured in paraffin solution (density of 0.775 g/cm^3) according to Archimedes' principle.

Raman spectra were carried out on a LabRam HR laser confocal Raman Spectroscopy (Made by HORIBA, Japan) with a laser wavelength of 532 nm.

X-ray photoelectron spectroscopy (XPS) was performed under a very high vacuum on the model ESCALAB 250 (USA). The XPS peaks were calibrated regarding C and O elements.

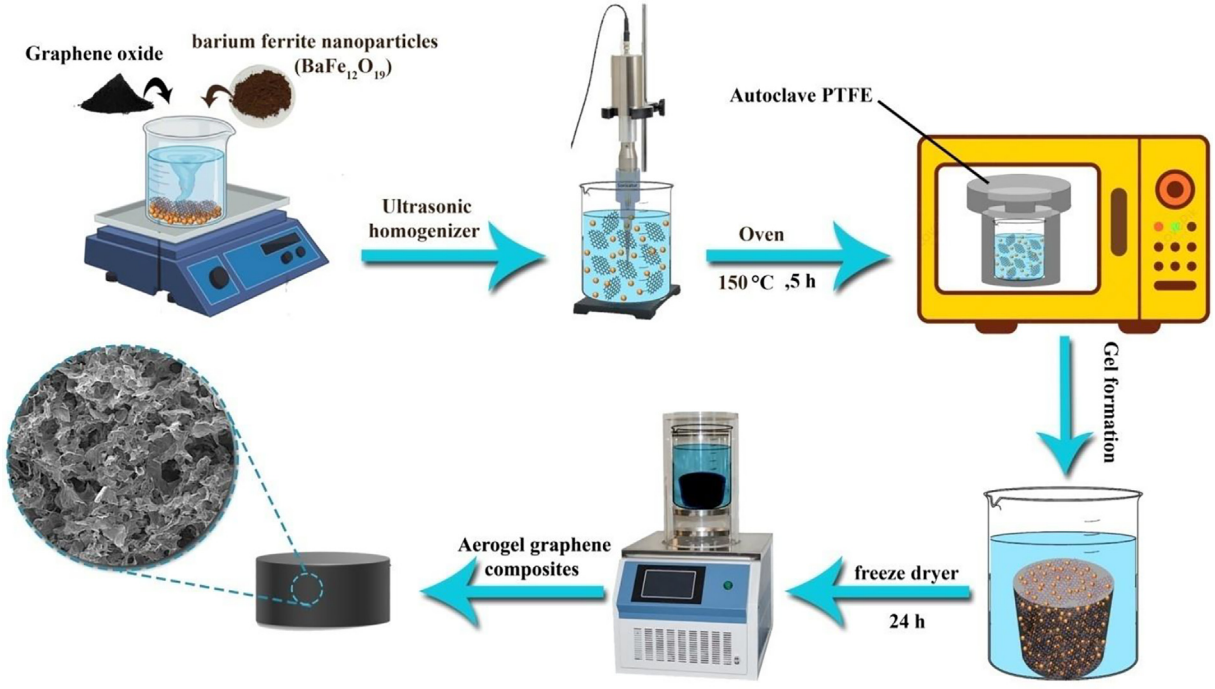

Fig. 1 Schematic of the synthesis step of graphene oxide/barium ferrite aerogels composite.

Table 2 Properties of the samples.

Sample	Barium ferrite nanoparticle content ($BaFe_{12}O_{19}$)		Graphene oxide content (GO)		GO:$BaFe_{12}O_{19}$	Sample code
	Weight (g)	Weight percentage (%)	Weight (g)	Weight percentage (%)	ratio	
GO	–	–	–	–	–	GO
BF	0.250	100	0	0	0:1	BF
1	0	0	0.25	100	1:0	GA
2	0.080	25	0.25	75	3:1	3GO/BF
3	0.125	33	0.25	67	2:1	2GO/BF
4	0.166	40	0.25	60	3:2	3GO/2BF
5	0.250	50	0.25	50	1:1	GO/BF
6	0.375	60	0.25	40	2:3	2GO/3BF
7	0.500	67	0.25	33	1:2	GO/2BF

Thermal stability using thermal gravimetric analysis (TGA) of Labsys Evo device at room temperature up to 800 °C with a rate of 10 °C/min under argon atmosphere (Shi et al., 2023). Differential scanning calorimetry (DSC, DSC131 evo) device was applied from room temperature to 600 °C at a rate of 10 °C/min under air atmosphere.

The magnetic properties of the samples, including hysteresis curves, saturation magnetization, and coercive field were evaluated using a vibrating sample magnetometer (Meghntis Daghigh Kavir, made in Iran) device in a 1.5 Tesla field (Khorshidi et al., 2022; Marras et al., 2008; Song et al., 2023; Xu and Liu, 2023; Ngafwan et al., 2021).

PVAN5222A device (Malaysia) was used with a frequency range of 0–26 GHz to measure the dielectric constant and magnetic permittivity of the samples.

Field emission scanning electron microscope (FE-SEM) (MIRA3, TESCAN Co.) was used with a resolution of 1.5 nm at a voltage of 15 kV (Fu et al., 2020; Suanto et al., 2022) to explore the morphology (Raya et al., 2022; Jasim et al., 2022; Guo et al., 2022; Fu et al., 2020; Bokov et al., 2021) of the barium ferrite nanoparticles, graphene oxide sheets, and distribution of barium ferrite nanoparticles onto the graphene oxide sheets.

3. Results and their analysis

3.1. Examining the XRD Patterns

Fig. 2a indicates the XRD pattern of graphene oxide (GO) powder. Two peaks at 2θ of 12° and 43° represent the (001) and (100) planes of GO sheets, respectively (Kumar et al., 2019; Ain et al., 2019). Also, Fig. 2a depicts the XRD pattern of graphene oxide aerogel. GO aerogel has two reflections at 23.98° and 42.92°, being related to (002) and (100) planes, respectively (Pavithra et al., 2017; Jiao et al., 2017). Since the structure of GO aerogel differs from that of GO powder in terms of inter-plane distance, and the distance between the GO aerogel planes is lower than that of GO powder due to the reduction of C═C functional groups, the diffraction angle of GO aerogel grows; accordingly, the diffraction at 12° of GO nanopowders is transferred to 24° in GO aerogel (Fig. 2a), but the diffraction of (100) plane does not change in the aerogel process (Jiao et al., 2017).

Fig. 2b displays the XRD pattern of barium ferrite nanoparticles. The XRD pattern indicates the presence of a barium ferrite phase with a hexagonal crystalline system matching the reference code of 078-0.133 and iron oxide impurity matching the JCPDS No. 013-0534.

The diffraction emerging at angles of 30.485, 32.326, 37.252, 40.501, 42.614, 55.318, 56.847, 60.282, 63.384, 67.662, 72.961, and 77.971° are related to planes of (110), (107), (114), (203), (205), (206), (217), (2011), (2012), (220), (2014), (317), and (405) for the barium ferrite nanoparticles structure. The peaks observed at 2θ of 24.299, 33.280, 35.744, 40.972, 49.555, 62.540, 64.080, 72.033, and 75.515° are attributed to (012), (104), (110), (113), (024), (214), (300), (1010), and (220) planes of iron oxide phase (Fe_2O_3).

To determine the crystallite size, the Scherrer equation was used. The crystallite size of the barium ferrite nanoparticles, using this relation, was found at 15–48 nm. Also, the crystallite size of iron oxide was achieved by 28–60 nm.

Also, Fig. 2b reveals the XRD pattern of the GO/2BF graphene oxide aerogel composite sample. As seen, most diffractions of barium ferrite nanoparticles, as explained earlier, exist in this XRD pattern. Also, the presence of the wide diffraction within the 2θ range of 20° confirms the presence of GO aerogel. The XRD pattern of other synthesized samples is also similar to that of the GO/2BF sample, with the difference that in some samples, the intensity of the barium ferrite nanoparticles peaks has diminished. This can be attributed to less separation of GO planes from each other as well as the low BF nanoparticles to GO ratio. In Fig. S1 of the appendix, the XRD patterns of all samples, including GO/2BF, 2GO/3BF, GO/BF, 3GO/2BF, 2GO/BF, and 3GO/BF are shown.

3.2. Fourier transform infrared (FTIR) spectroscopy

Fig. 3 displays the results of FTIR of the pure barium ferrite nanoparticles, GO, and GO/BF nanocomposites. In the FTIR analysis of barium ferrite nanoparticles, the presence of two bands at 578 cm^{-1} and 432 cm^{-1} is related to oxygen-metal (M—O) bonds (Feng et al., 2017). Based on Fig. 3, the band at 432 cm^{-1} is related to Fe—O bonds at octahedral sites in ferrite lattice (Forushani et al., 2023a), while the wavenumber of 578 cm^{-1} is associated with the M—O bonds at tetrahedral sites in the hexagonal structure of the barium ferrite. Thus, FTIR analysis confirms the presence of hexagonal barium ferrite nanoparticles (Vinay et al., 2018; Ghzaiel et al., 2016).

In the FTIR analysis related to GO and GO aerogel, the presence of a wide peak at 3422 cm^{-1} is related to stretching vibrations of O—H in the GO sheets (Gong et al., 2015). Also,

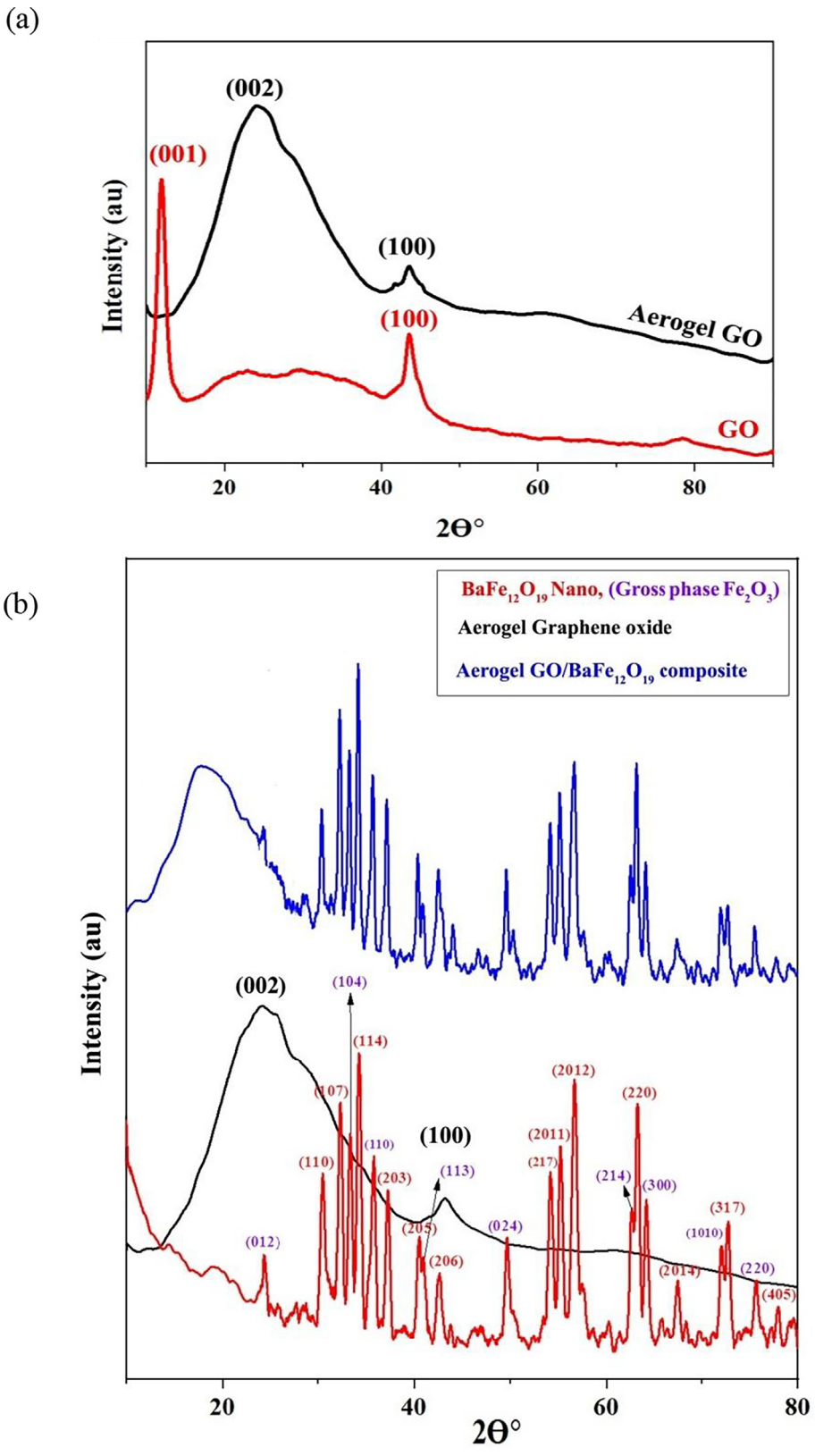

Fig. 2 XRD pattern of (a) graphene oxide (GO) and graphene oxide aerogel (GA) (b) Barium ferrite nanoparticles, graphene oxide aerogel (GA) and, composite of graphene oxide aerogel /barium ferrite nanoparticles.

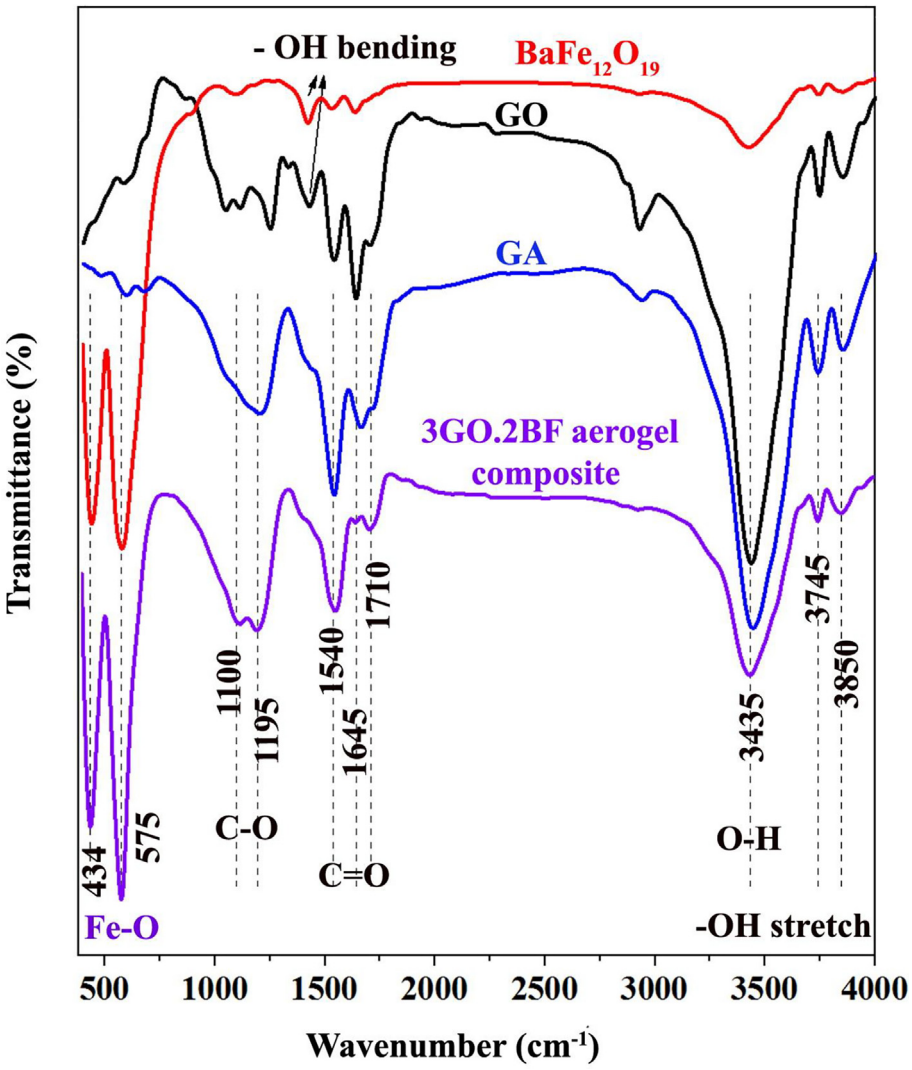

Fig. 3 FTIR spectroscopy of the GO nanopowders, graphene oxide aerogel (GA) and GO/barium nanocomposites.

the band at 2920 cm^{-1} indicates aliphatic stretching vibrations of C—H_2 bonds (Zhao et al., 2023; Marras et al., 2008; Zhang et al., 2016; Wang et al., 2021; Zhang et al., 2022). The band at 1716 cm^{-1} confirms the presence of C═O stretching vibrations of the carboxylic group, while the peak at 1650 cm^{-1} originates from the bending modes of water molecules integrated into the GO structure (Fig. 3). In the FTIR spectrum of GO/BF nanocomposite, the wavenumber of 1211 cm^{-1} is related to the C—O stretching vibrations of GO nanosheets. FTIR diagrams of all samples are shown in Fig. S2 of the Appendix.

3.3. X-ray photoelectron spectroscopy (XPS) analysis

Fig. 4 shows the XPS analysis of a graphene oxide/barium ferrite aerogel composite (3GO/2BF sample). Based on these curves, the peaks that originate from constituents of this composite, namely carbon, oxygen, iron, and barium, are observed. Fig. 4a is related to the full XPS spectrum of graphene oxide/barium ferrite aerogel composite and the elements in it are specified. In Fig. 4b, the peak of 779.35 eV corresponds to Ba 3d and Ba $3d_{5/2}$ and the peak of 793.45 eV is related to Ba $3d_{3/2}$ of the barium element. Fig. 4c is related to the iron element (in BF nanoparticles), which has two peaks of 709.75 eV and 723.25 eV corresponding to Fe $2p_{3/2}$ and Fe $2p_{1/2}$, respectively (Anand et al., 2020; He et al., 2023).

Fig. 4d shows the spectrum of oxygen (O 1s) at the binding energy of 530.55 eV, which can be quantitatively distinguished into three different parts. The oxygen is related to metal oxides with a binding energy of 528.91 eV, metal carbonates with a binding energy of 530.98 eV and C—O located at 535.38 eV. Fig. 4e shows the C 1s peaks with a binding energy of 283.55 eV, which can be quantitatively divided into two species, which are C—C peak at 283.47 eV and C—O—C with the binding energy of 286.01 eV (Anand et al., 2020; He et al., 2023). Fig. 4f shows other peaks of barium elements corresponding to the 4d, 5s, and 5p orbitals transition. More information, including the surface area and content of each element, is listed in Table 3.

3.4. Raman spectrum analysis

Fig. 5 illustrates the Raman spectra obtained using a laser wavelength of 532 nm for barium ferrite nanoparticles, graphene oxide sheets, and graphene oxide nanoparticles/barium

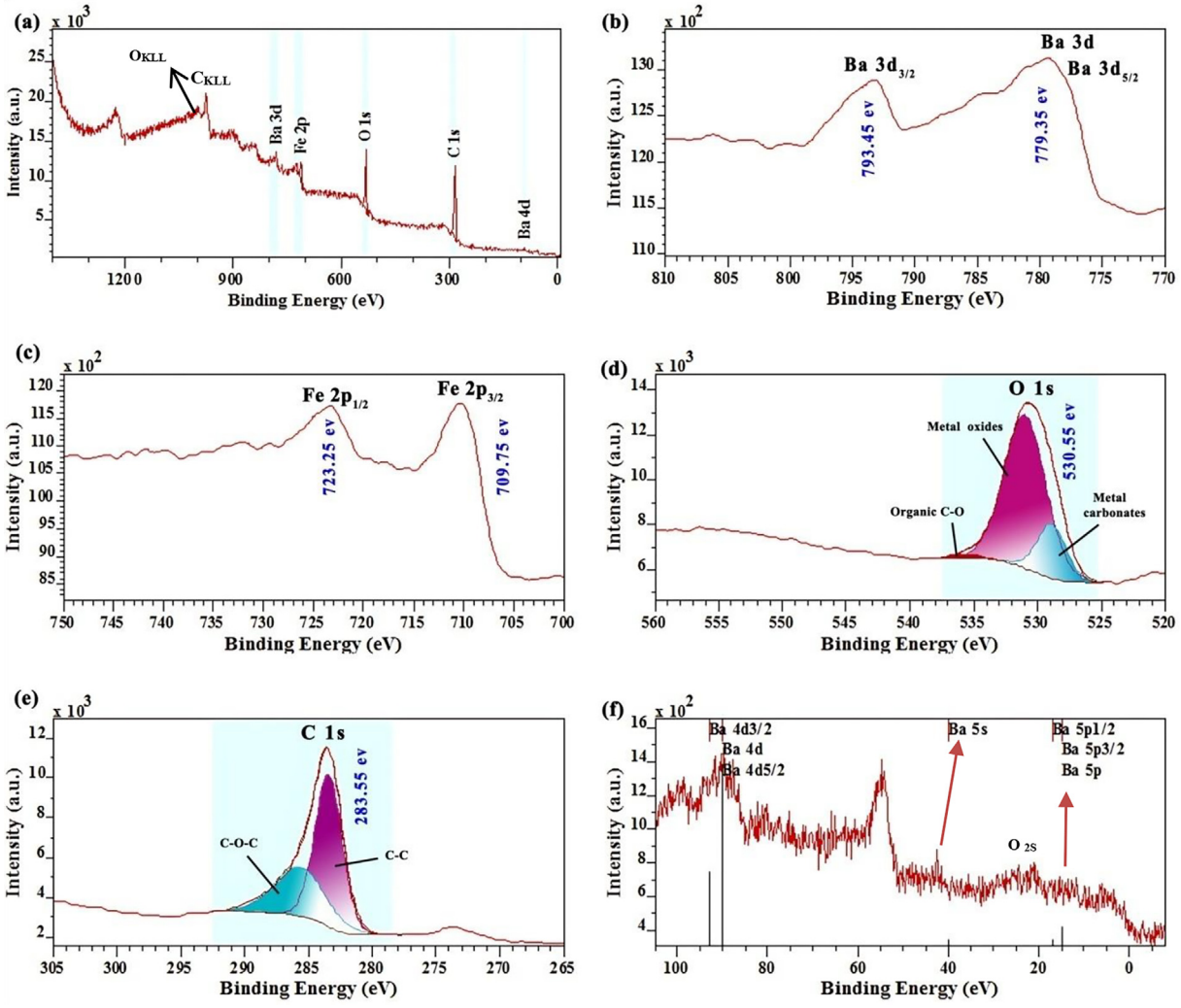

Fig. 4 Full XPS spectra (a) 3GO/2BF Aerogel, (b) Barium (Ba 3d) element, (c) iron element, (d) Oxygen (O 1s) element, (e) Carbon (C 1s) element, (f) Barium (Ba 4d and Ba 5p) element.

Table 3 Weight atomic ratio, FWHM, and peak areas of the elemental composition of the AGO/BF by XPS analysis.

Elements		Position	FWHM	Area	Wt.%	
C 1s		283.55	3.130	3447.56	74.86	
O 1s		530.55	4.531	3073.82	23.44	
Fe 2p	Fe $2p_{3/2}$	709.75	4.005	710.69	71.23	1.38
	Fe $2p_{1/2}$	723.25	4.030	287.11	28.77	
Ba 3d	Ba $3d_{5/2}$	779.35	5.604	404.06	68.24	0.32
	Ba $3d_{3/2}$	793.45	4.500	188.02	31.76	

ferrite composite aerogel (sample 3GO.2BF). For a strong Raman signal, a shorter wavelength (532 nm) is more advantageous as the intensity of the Raman band is inversely proportional to the fourth power of the excitation wavelength (Hanson et al., 2016).

Two distinct bands at 1353 cm^{-1} (D-band) and 1586 cm^{-1} (G-band) (Budi et al., 2022; Salahdin et al., 2022) for graphene oxide (GO) indicate that after the fabrication of the graphene oxide composite aerogel, the D band remains unchanged while the peak of the G-band shifts to 1598 cm^{-1} (Boruah et al., 2017). The relative intensity ratio of I_D/I_G was calculated to be 0.89 for graphene oxide and 1.04 for the graphene oxide composite aerogel, representing an increase from 0.89 to 1.04, indicating the augmentation of defect points and structural changes (Hanson et al., 2016; Feng et al., 2022; Sun, 2023).

Furthermore, the peaks of the barium ferrite nanoparticles (red curve in Fig. 5) used in the fabrication of the graphene

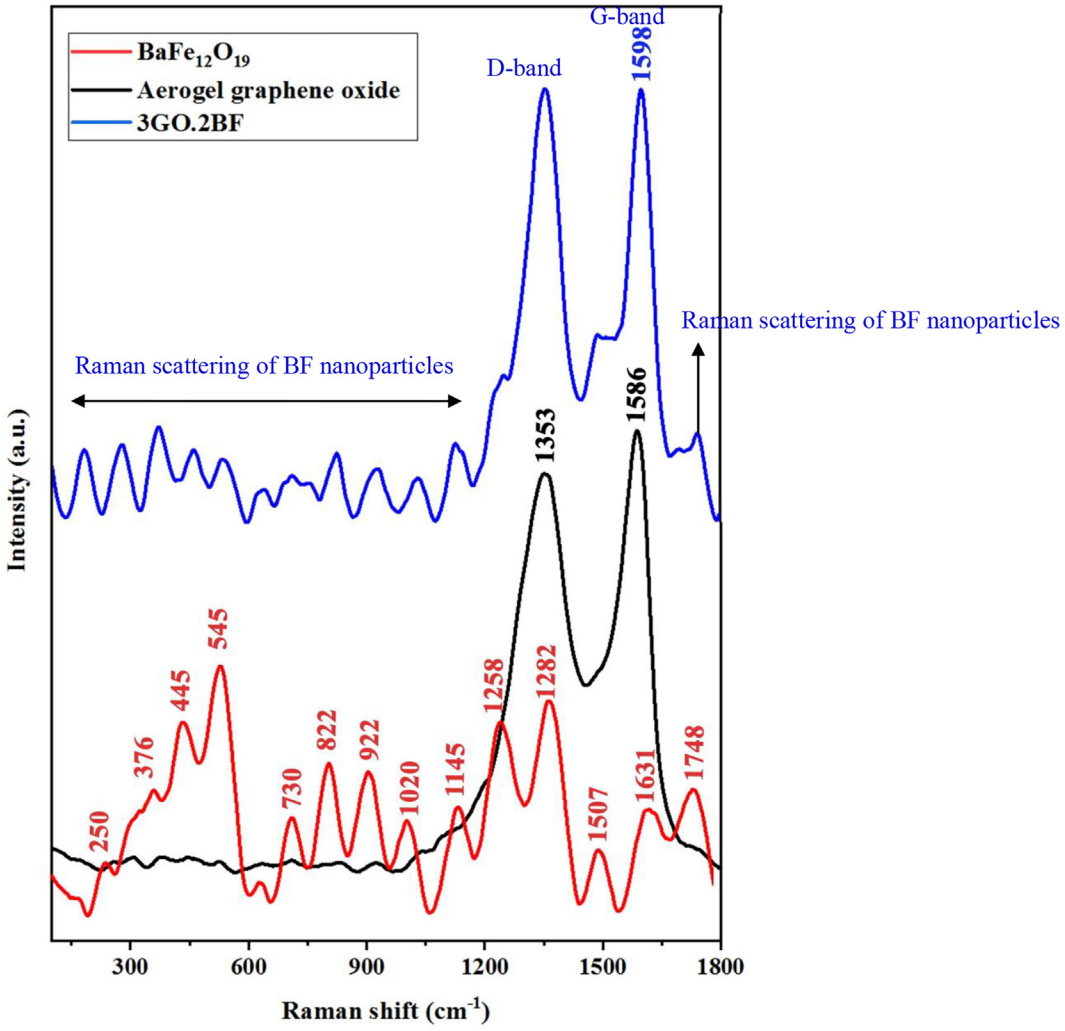

Fig. 5 Raman spectrum of $BaFe_{12}O_{19}$ (BF) nanoparticle (red), pure graphene oxide (GO) (black), and graphene oxide aerogel composite (3GO.2BF) (blue).

aerogel composite match the peaks of the 3GO.2BF aerogel composite sample (blue curve in Fig. 5).

3.5. Thermal stability analysis using TGA and DSC

Fig. 6 shows TGA and DSC analysis of pure graphene oxide aerogel and graphene oxide aerogel/barium ferrite (3GO.2BF) composite. By examining the thermal analysis (TGA) in the GA sample, it can be seen that from the temperature of 180 to 280 °C, a weight loss of 3.93% is seen due to the release of CO, CO_2 gas (Sun, 2023) and evaporation of adsorbed water (Kim et al., 2017). After that, the decomposition of the graphite substructure begins, which results in a greater weight loss for GO aerogel at temperatures higher than 400 °C (Du et al., 2023). Graphene oxide aerogel lost 11.4% of its weight up to a temperature of 800 °C (Fig. 6a), but, the 3GO.2BF sample shows a weight loss of 3.36%. thus, 3GO.2BF aerogel nanocomposite has higher thermal stability than pure GO aerogel (Fig. 6b).

Fig. 6(c,d) is related to DSC analysis from room temperatures to 600 °C for GA and 3GO.2BF samples. As indicated in both graphs, the endothermic part is related to the evaporation of water and the exothermic part is related to the oxidation of carbon in the samples. (Sun, 2023; Kim et al., 2017; Du et al., 2023; Gonçalves et al., 2020; Mazaheri Forushani et al., 2023; Zhang et al., 2022; Du et al., 2023; He et al., 2023).

3.6. Morphological examination

Fig. 7a reveals the FESEM image of the purchased GO powder. As seen in this figure, the GO morphology is planar. Expectedly, GO has a layered structure, where the thickness of the planes is 40–50 nm. Fig. 7b shows a FESEM image of barium ferrite nanoparticles. As observed, the structure of barium ferrite nanoparticles is hexagonal planar. Based on the images, the length of the planes is around 250 nm and its thickness is about 50 nm.

Based on the microscopic images in Fig. 8, the 3D structure of GO has been formed as interlinked twisted layers. According to Fig. 8a and b, the pores present in the aerogel are micrometric. Also, the pores are nonuniform, which may have happened due to drying the GO hydrogel method.

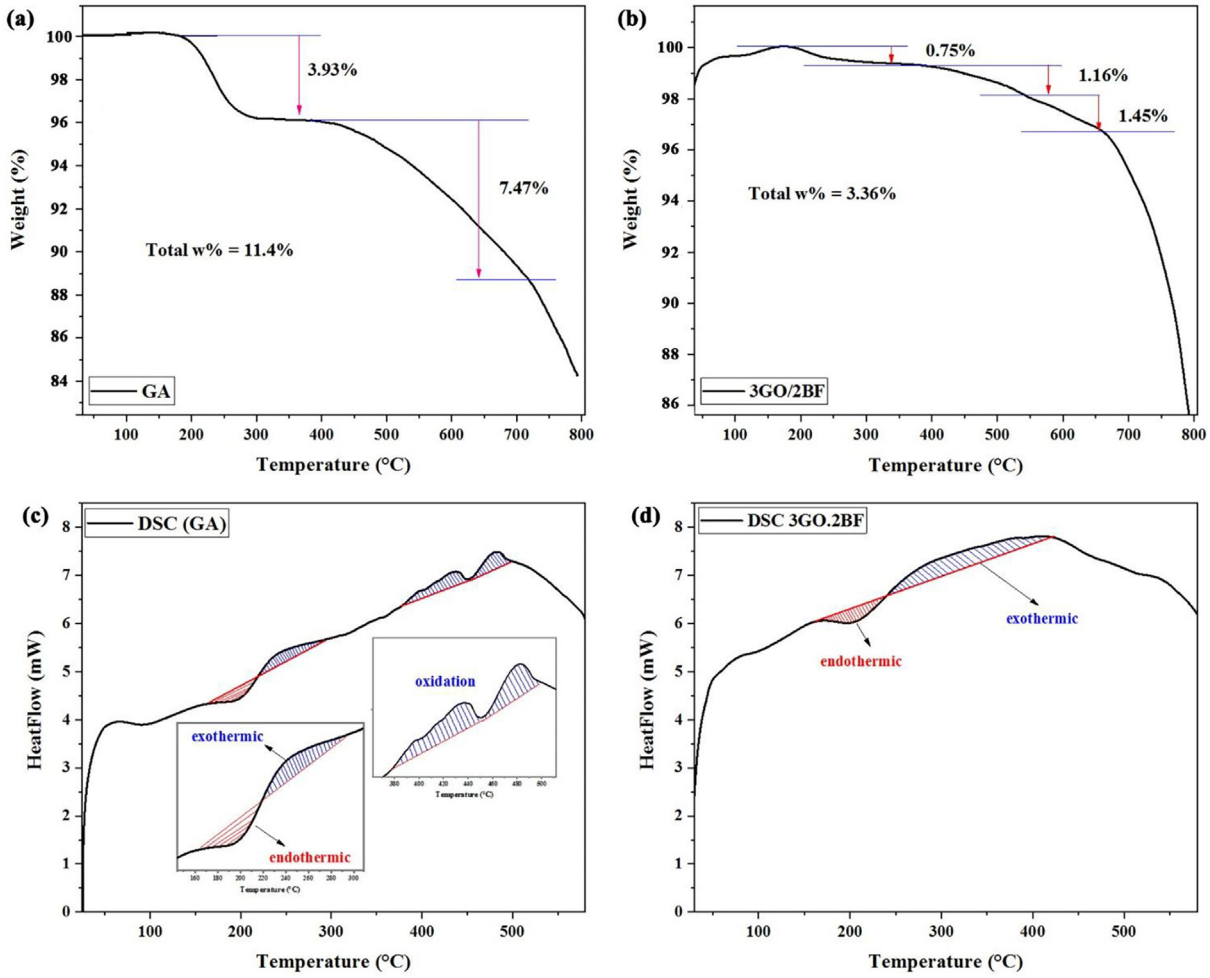

Fig. 6 TGA curves for (a) aerogel graphene oxide (b) sample 3GO.2BF. DSC curves for (c) aerogel graphene oxide (d) sample 3GO.2BF.

Fig. 8e-h reveals the FESEM images of GO aerogel /barium ferrite nanoparticles composite (3GO/2BF) with different magnifications. As observed, barium ferrite nanoparticles have been bonded to the GO planes randomly and due to van der Waals force. Barium ferrite nanoparticles have been attached and at some points agglomerated due to intrinsic magnetic properties, the small size of nanoparticles, and the use of a high weight percentage of BF nanoparticles.

It is expected that this agglomeration and nonuniform distribution on GO planes would not be useful for the absorption of electromagnetic waves since these conditions cause a reduction of magnetic loss on GO planes. Carefully inspecting these images, it is seen that in addition to GO planes, ferrite nanoparticles have also been linked at the edges of the planes, which is useful for enhancing the magnetism of aerogel composites. Also, the use of a very high percentage of barium ferrite nanoparticles causes the size of pores to diminish and the separation of GO planes to decline compared to previous samples. This elevation of weight percentage will be useful for the enhancement of saturation magnetization and the absorption of electromagnetic waves.

Fig. 8i reveals FESEM images and its EDS mapping of the graphene multiplanar surrounded by barium ferrite nanoparticles. This analysis shows the homogenous distribution of Fe and Ba elements from BF nanoparticles on the C element from GO sheets.

Fig. 9 shows the EDS diagrams of GO aerogel and GO aerogel/ barium ferrite nanoparticles composite. As seen, the level of carbon and oxygen indicates the presence of GO, while the existence of Fe and Ba elements reveals the presence of barium ferrite nanoparticles on the surface of GO nanosheets.

3.7. Magnetic behavior

The magnetic behavior of the samples was studied via a vibrational magnetometer. The main factors affecting the magnetic Hysteresis curve include ferrite phase content and the quality of the relationship between the magnetic phase and GO aerogel. Saturation magnetization can be associated with the fact that the distribution of barium ferrite nanoparticles within the homogeneous aerogel structure and at considerable distances from each other change the bipolar-bipolar interaction between BF nanoparticles affects the saturation magnetization. With the increase in the amount of barium ferrite nanoparticles in the sample, the saturation magnetization increases (bipolar-bipolar interaction functions) (He et al.,

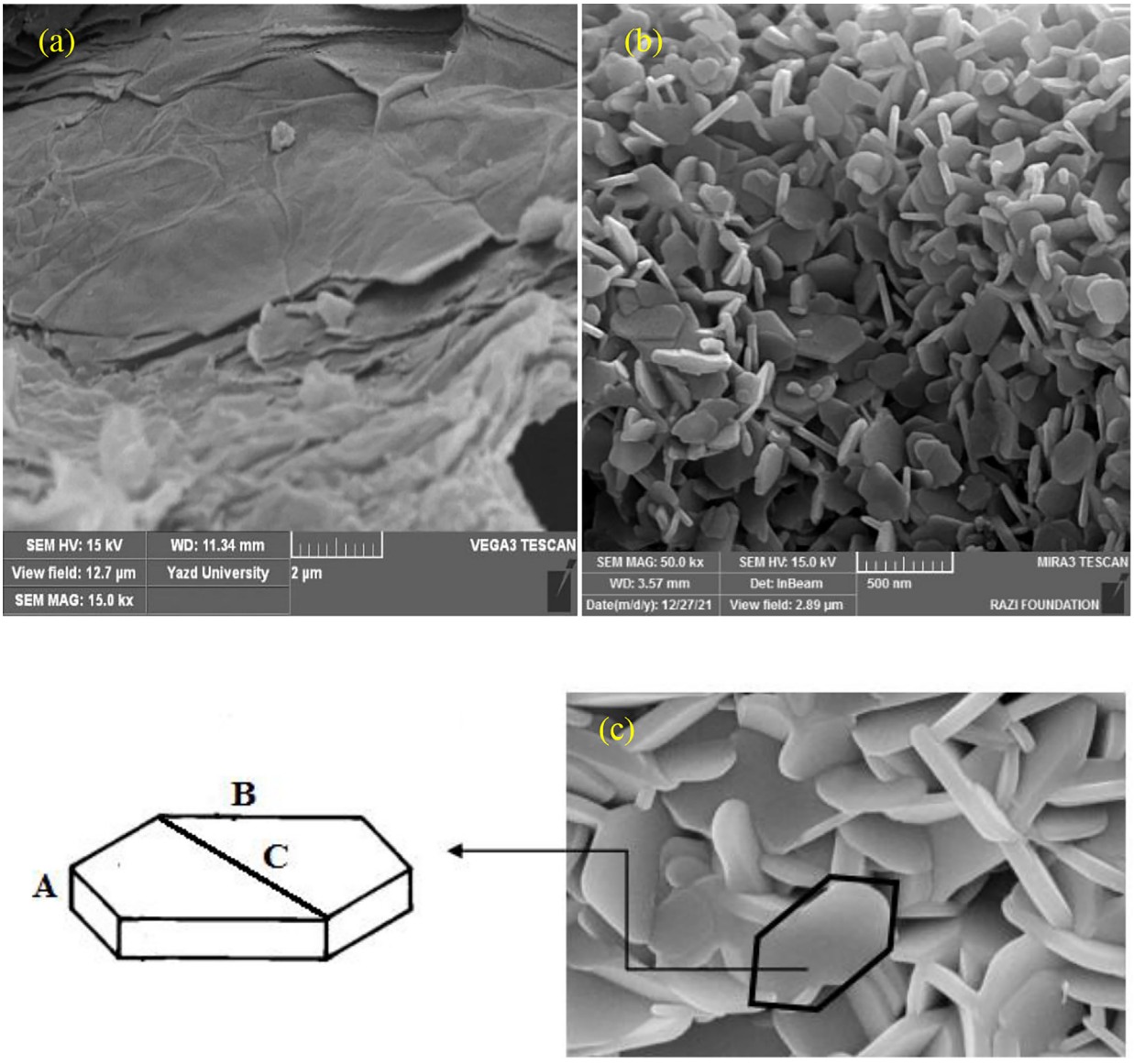

Fig. 7 SEM images of (a) GO, (b) barium ferrite nanoparticles, and (c) schematic of the hexagonal barium ferrite nanoparticles.

2023; Su et al., 2023; Zhao, 2022; Wang et al., 2020; Sharma et al., 2017).

According to Fig. 10 and Table 4, barium hexaferrite nanoparticles have hard ferrimagnetic properties. GO and GO aerogel does not have magnetic properties. With the increasing amount of barium ferrite nanoparticles in the samples, the magnetism of the samples grew due to the dense distribution of nanoparticles on the GO nanosheets with an increase in the dipole–dipole bonds. Meanwhile, in the samples, with an increase in the barium ferrite nanoparticles, as previously observed in the XRD pattern, there is an iron oxide impurity phase. This impurity has led to reduced saturation magnetization of barium ferrite nanoparticles compared to the pure state. In the GO aerogels/ barium ferrite nanoparticles composite, the saturation magnetization depends on the amount of barium ferrite nanoparticles. The lower the percentage of barium ferrite nanoparticles, the less saturation magnetization would become in proportion with the percentage. The magnetization of 3GO/BF, 2GO/BF, and 3GO/2BF samples is close to each other, where an increase in the barium ferrite nanoparticles does not have much effect on their saturation magnetization. In the GO/BF, 2GO/BF, and GO/2BF samples, with increasing the amount of barium ferrite nanoparticles, the magnetization grows from 5–7 emu/g to 13–29 emu/g. These results suggest that with a 50 wt% increase in the barium ferrite nanoparticles, the effects of magnetization on aerogel composite become evident, and gradually with an increase in the weight percentage of nanoparticles, the magnetic properties of the composite have also been enhanced.

According to Table 4 and Fig. 10, the most coercivity of nanocomposite (H_c = 3795.16–4091.55 Oe) was enhanced as compared to pure BF nanoparticles (H_c = 3360.46 Oe). The reduction in the Hc of 3GO/2BF can be due to the separation of $BaFe_{12}O_{19}$ nanoparticles by GO nanosheets (He et al., 2023;

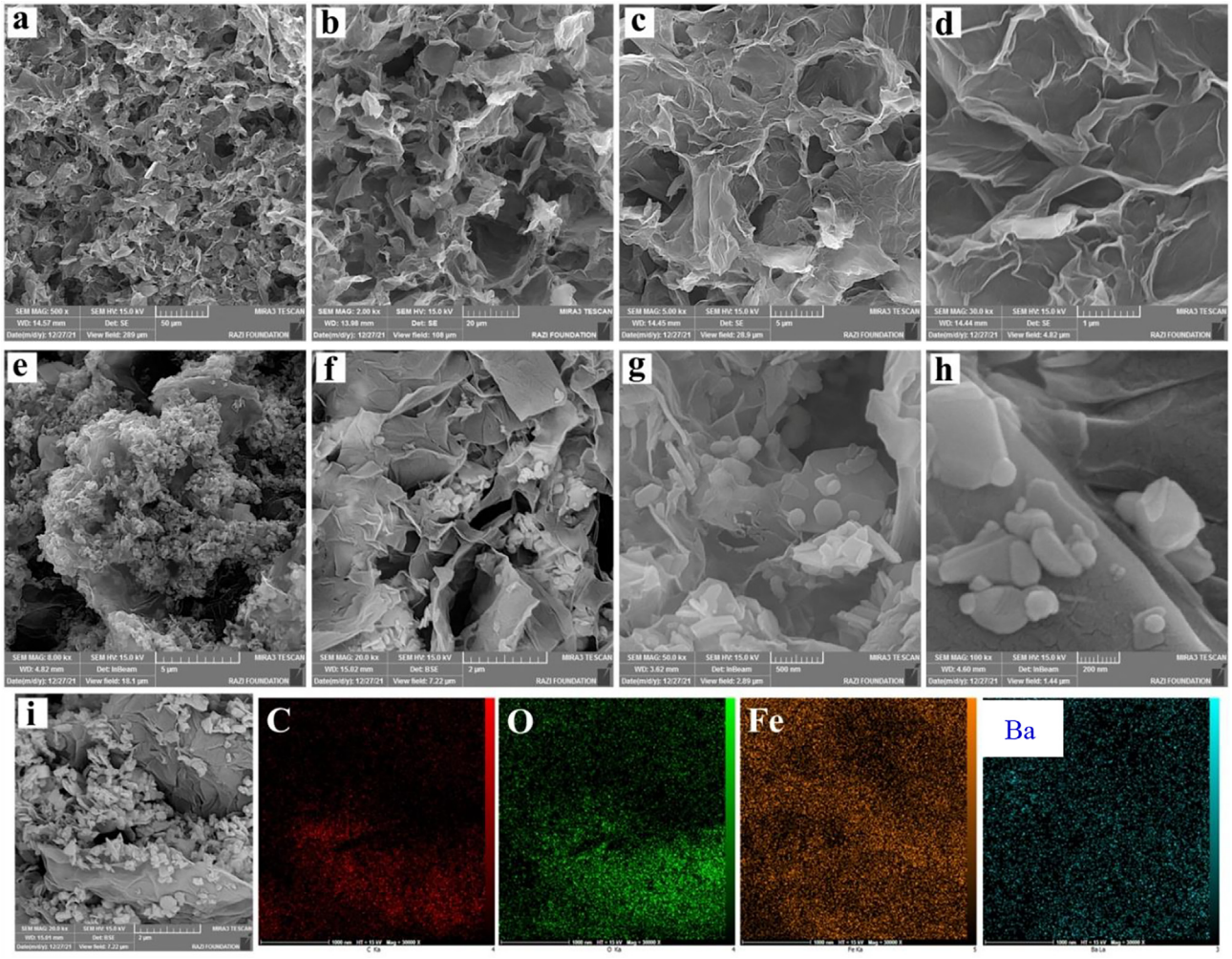

Fig. 8 (a–d) images of graphene oxide aerogel (GA) with different magnifications, (e–h) images of graphene oxide aerogel/ barium ferrite nanoparticles composite (3GO/2BF) as well as arrangement of nanoparticles onto the GO planes with different magnifications, (i) SEM and EDS mapping of GO/ barium ferrite aerogel.

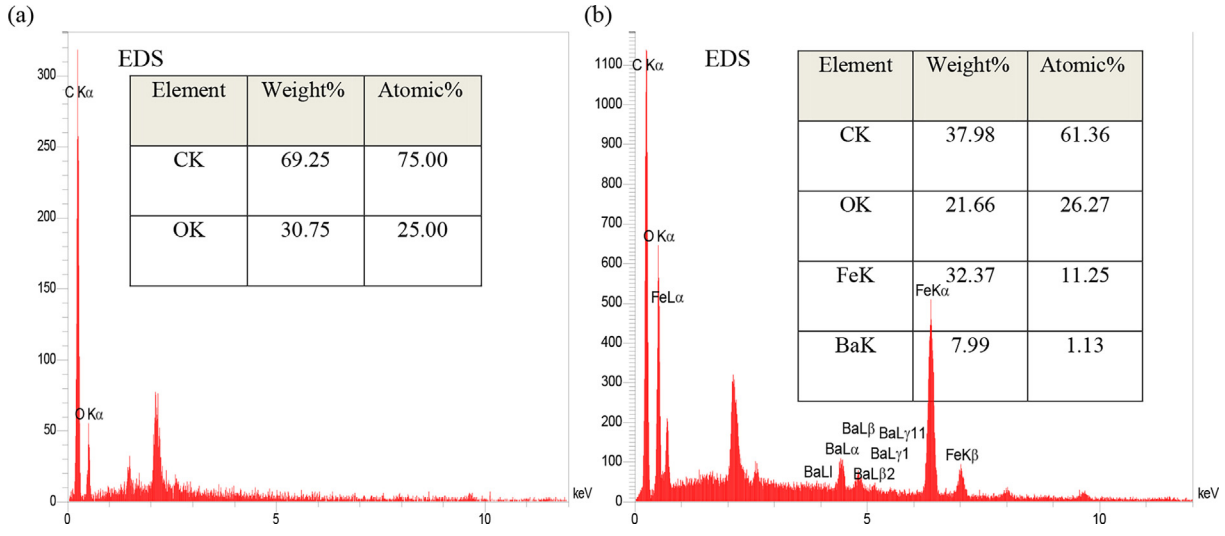

Fig. 9 EDS analysis of (a) graphene oxide aerogel, (b) GO aerogel composite with barium ferrite nanoparticles additives.

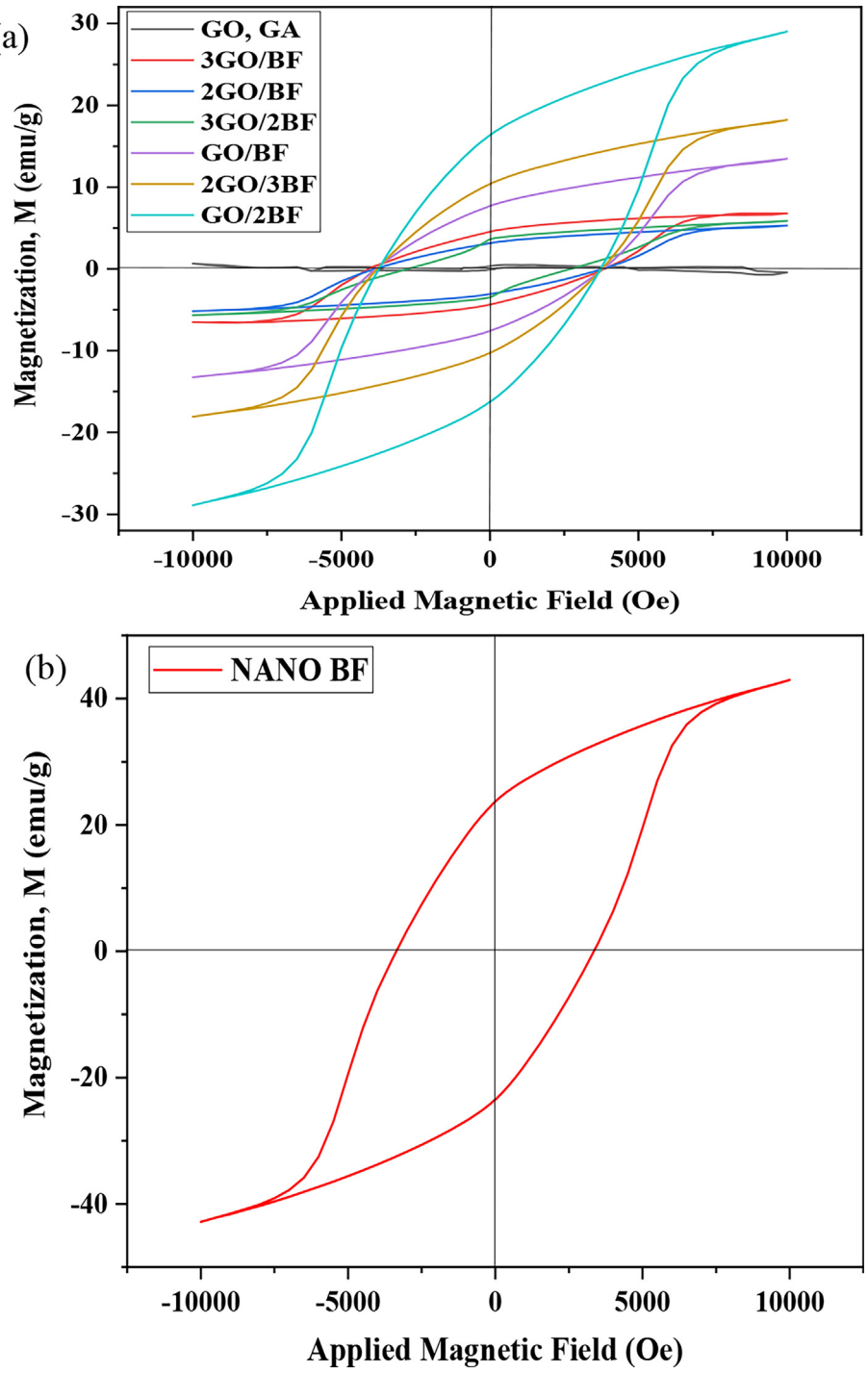

Fig. 10 Hysteresis loop of (a) pure go,graphene oxide aerogel (GA) and GO/BF nanocomposites, (b) the utilized barium ferrite nanoparticles.

Su et al., 2023; Zhao, 2022; Wang et al., 2020; Sharma et al., 2017).

3.8. EM wave behavior

In the absorption of electromagnetic waves in GO/BF composite, the most important part is examining the magnetic losses and dielectric losses of the material. If these losses are high and their values get close to each other, the maximum absorption would occur in the electromagnetic absorbent.

According to Relation (1) (Nanni and Valentini, 2011):

$$\mu* = \mu' - j\mu'' \quad (1)$$

where the real component (μ') is the stored energy and magnetic permittivity, while the imaginary component (''μ) is the lost energy or magnetic losses.

Table 4 Magnetic properties of the samples.

	Magnetization (emu/g)	Coercivity (Oe)
Graphene oxide (GO)	0	–
Barium ferrite nanoparticles (BF)	42.94	3360.46
Graphene oxide aerogel (GA)	0	–
3GO/BF	6.78	4091.55
2GO/BF	5.22	3865.20
3GO/2BF	5.87	2765.85
GO/BF	13	3844.28
2GO/3BF	18	3795.16
GO/2BF	29	3737.75

$$\varepsilon* = \varepsilon' - j\varepsilon'' \tag{2}$$

In Eq. (2), the real part, indicated by ε', is called the dielectric coefficient, and determines the amount of electrostatic energy stored in the volume unit of the material at the applied field. The imaginary part, represented by ε'', characterizes th losses of the energy controlled through a delay in the polarization as soon as the wave propagates at the time of crossing the material (Vinay et al., 2018). The tangent of the magnetic losses is also defined as follows (Vinay et al., 2018):

$$\tan\delta_\mu = \frac{\mu''}{\mu'} \tag{3}$$

$$\tan\delta_\mu = \tan\delta_h + \tan\delta_e + \tan\delta_r \tag{4}$$

In this definition, $\tan\delta_h$ represents the tangent of hysteresis losses, and $\tan\delta_e$ denotes the residual losses (severe losses are often prevailing at high frequencies), while $\tan\delta_r$ is the tangent of vortexed flow losses (Vinay et al., 2018).

Also, to express the dielectric losses from the dielectric loss tangent, Relation (5) is used (Ghzaiel et al., 2016, Yusof, 2004).

$$\tan\delta_\varepsilon = \frac{\varepsilon''}{\varepsilon'} \tag{5}$$

The larger the imaginary part of the magnetic permittivity and the imaginary part of the dielectric constant, and the lower their real parts, the greater the magnetic and dielectric losses will be in that material, which is more suitable. According to impedance matching principles, when the magnetic permittivity becomes equal to the dielectric constant of a material, there would be no reflection, and the absorption is in the best state. Also, if the tangent of magnetic losses as well as the tangent of dielectric losses is close to each other, impedance matching occurs and the material has good absorption.

To explore the absorptivity of the electromagnetic waves by the GO aerogel nanocomposites containing magnetic nanoparticles, the schematics of the input electromagnetic wave and its processes were drawn in Fig. 11.

When the input wave hits the nanocomposite, three states occur reflection, absorption, and transmission. Since the samples have GO aerogel and GO planes in them are three-dimensional and have pores, when the electromagnetic wave enters and hits the surface of the sample, due to the presence of pores in aerogel, it penetrates the sample. Then, with a frequent strike to the GO planes, the electromagnetic wave energy changes into heat energy, whereby the electromagnetic wave is absorbed into the sample.

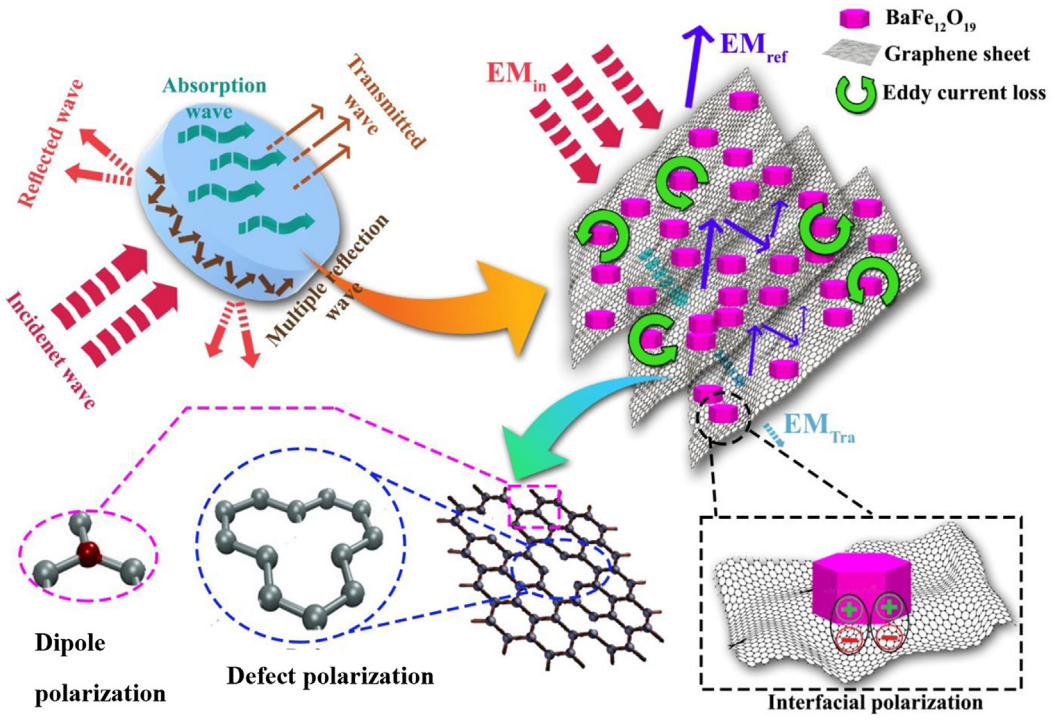

Fig. 11 Schematic of the mechanism of interactions of incident electromagnetic waves with the nanocomposites.

At the impact of electromagnetic waves on the GO planes, to which barium ferrite nanoparticles have been bonded, as previously observed in FESEM images, two states occur so that the electromagnetic wave would be absorbed. The first state is dielectric losses on the GO planes due to having electric conductivity and electric permittivity, which causes absorption of EM waves with the movement of electrons on the planes and their transfer to other graphene planes. Also, due to the occurrence of superficial polarization processes as well as the dipole polarization on the GO planes, EM wave absorption occurs.

The barium ferrite nanoparticles linked to GO planes cause the development of magnetic losses at the time of hitting the electromagnetic wave to them, whereby wave absorption occurs in this state. Losses of vortexed flow are one of the three parts of magnetic loss that cause the absorption of electromagnetic waves (Mazaheri Forushani et al., 2023; Sharma et al., 2017).

In the GO aerogel nanocomposites containing barium ferrite nanoparticles, due to the 3D state of graphene planes and the separation that had occurred in the graphene planes (confirmed by a wide peak at 2theta of 24° in the XRD pattern of GO aerogel) and observed in the FESEM micrograph, the dielectric losses resulting from this planar structure will be high. The presence of pores in nanocomposites causes multiple impacts of EM waves onto the graphene planes and enhances the role of dielectric losses in the absorption of electromagnetic waves.

Nevertheless, the conditions are different for magnetic losses. This is because the random and nonuniform distribution of barium ferrite nanoparticles (according to Fig. 8) causes a reduction of magnetic losses. Meanwhile, based on the XRD pattern, the detected impure phase (α-Fe_2O_3) causes a reduction of magnetic losses. These aforementioned factors affect the magnetic losses and cause a reduction of these losses compared to the dielectric losses.

According to Fig. 12, the imaginary part of the magnetic permittivity of all samples is close to zero, while the real part of the magnetic permittivity is larger than that. Thus, in the samples, the magnetic losses are not greater. The imaginary part of the dielectric constant is close to the real part of the dielectric constant; so in the composite samples, dielectric losses are better than magnetic losses. The values of the tangent of the magnetic losses are close to each other. Thus, some samples can be used as electromagnetic wave absorbents.

Adjustment of electric conductivity is one of the important parameters in creating EM wave absorbent materials. Increase in electric conductivity results in increased losses in the vortexed flow and conductivity. Meanwhile, with an elevation of electric conductivity, the extent of apparent resistance coupling between the environment and absorbent decreases. Thus, the depth of shells will be very small, and almost all electromagnetic waves will be reflected by the surface (Forushani et al., 2023b; Nanni and Valentini, 2011; Wang, 2015).

An increase in the electric conductivity leads to an enhancement in the losses of vortexed flow and conductivity. If a conductive material is placed in an alternating magnetic field, an induction current would be created in it. This current, which scatters the energy, is called eddy current loss. The extent of eddy current losses can be shown at frequencies with low magnetic current density with eddy current loss coefficient. For a sheet with "d" thickness and electric conductivity of σ, the eddy current loss coefficient (e) is expressed by Eq. (6) (Yang et al., 2016).

$$e = \frac{4\pi^2 \mu_0 d^2 \sigma}{3} \tag{6}$$

Also, if magnetic losses are only a result of eddy current loss, the C_0 constant, which is defined in Relation (7), should remain constant (Zhang and Cao, 2012).

$$C_0 = \mu'' \sqrt{\mu} f^{-1} = \frac{2}{3} \pi \mu_0 \sigma d^2 \tag{7}$$

Using real electric permittivity data ($\acute{\varepsilon}$), determined based on the output of the VNA device, the conductivity values (σ_{AC}) can be calculated using Eqs. (8) and (9):

$$\sigma AC\ (S/m) = 2f\pi\varepsilon 0\ \varepsilon'' \tag{8}$$

$$\omega = 2f\pi \tag{9}$$

Here, ω represents the frequency and ε_0 denotes the electric permittivity constant in vacuum, which is equal to 8.854×10^{-12} F/m, and e is the Neper number which is equal to 2.718 (Feher, 2009).

Also, to calculate the electromagnetic wave absorptivity in an absorbent, it is common to use the reflection loss parameter, which is obtained from Relation (10) (Ellwood and Legg, 1937).

$$|RL|(dB) = 20log_{10}|R| = 20log_{10}\left|\frac{Z_A - Z_0}{Z_A + Z_0}\right| \tag{10}$$

where Z_0 represents the free space impedance, defined as follows:

$$Z_0 = \sqrt{\frac{\mu_0}{\varepsilon_0}} \tag{11}$$

$$Z_A = \sqrt{\frac{\mu_A}{\varepsilon_A}} \tag{12}$$

and $Z_A$denotes the absorbent impedance, defined as follows:

Where the relative dielectric constant "ε_A" and relative magnetic permittivity "μ_A" is frequency dependent.

Also, to calculate the absorbent impedance in the normalized state, an absorbent model with a metal background is used in which case the absorbent impedance will be expressed as an Eq. (13)

$$Z_{RAM} = Z_{in} = Z_0 \sqrt{\frac{\mu_r}{\varepsilon_r}} \tanh\left(j\,\frac{2\pi fd}{c}\sqrt{\mu_r \varepsilon_r}\right) \tag{13}$$

where μ_r and ε_r represent the mixed magnetic permittivity and mixed dielectric permittivity of the material, respectively. Also, Z_0 is the impedance of free space, Z_{RAM} denotes the input impedance of the interface of composite/ free space, c is the speed of light in vacuum, f denotes the frequency of the impacted wave, and d is the sample thickness.

Based on Fig. 13a, the conductivity of the GA sample is higher than that of other samples due to the 3D state of GO planes in the GO aerogel. In the GO aerogel composites, due to the addition of non-conductive barium ferrite nanoparticles, the electric conductivity is lower than that of GO aerogel. Nevertheless, overall the conductivity of the samples has grown slightly with the frequency elevation.

According to Fig. 13b, for an increase in the eddy current losses, the absorbent should have a high thickness and electric

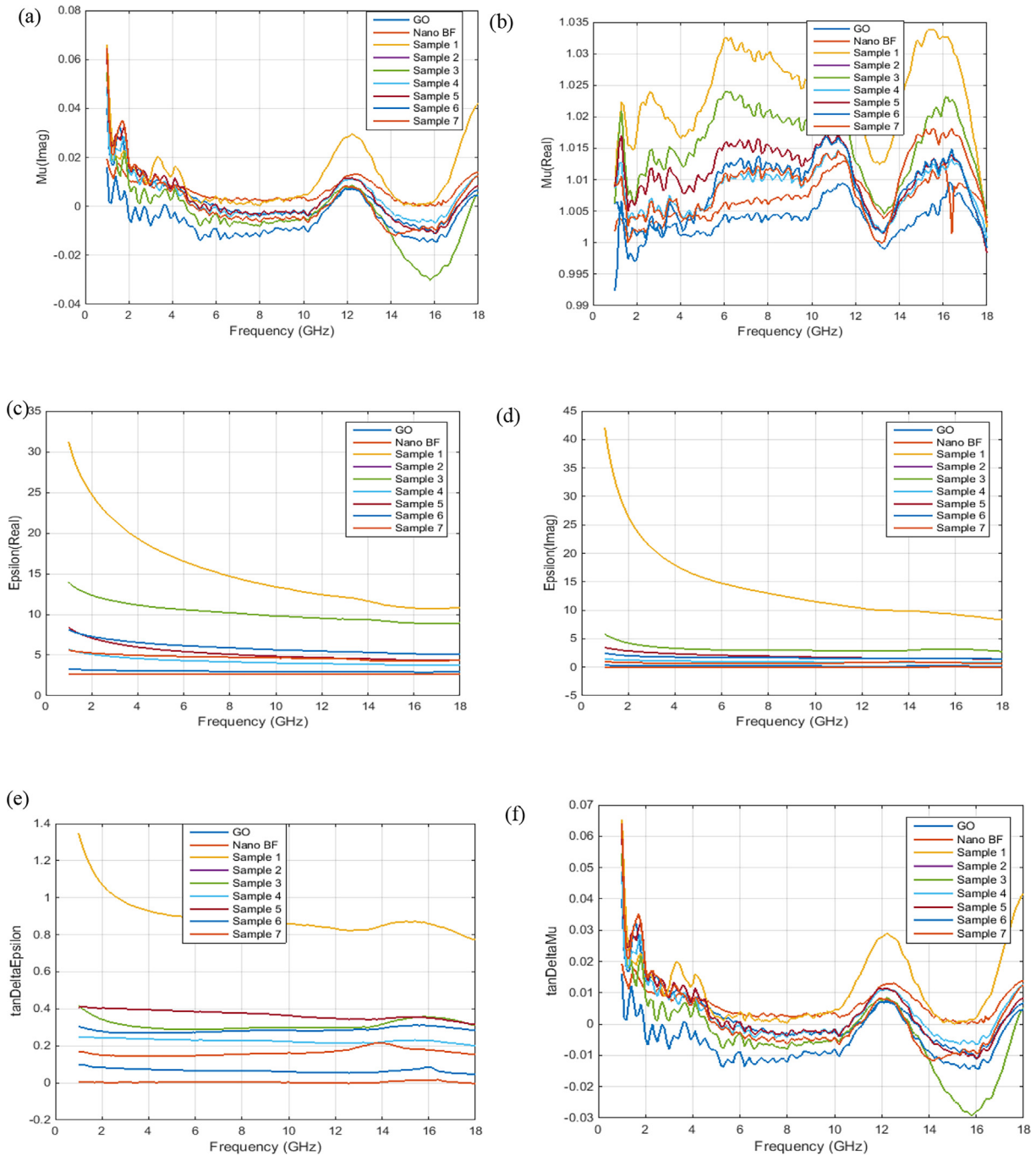

Fig. 12 A) imaginary part of magnetic permittivity, b) real part of magnetic permittivity, c) imaginary part of dielectric constant, d) real part of the dielectric constant, e) tangent of magnetic losses, and f) tangent of the dielectric losses. go and sample 1 is graphene oxide nanopowders and graphene oxide aerogel.

conductivity. Nevertheless, materials with high electric conductivity have a tendency to create unstable magnetic permittivity at high frequencies, which limits their usage at high frequencies such as X-band. If the magnetic losses are only due to eddy current losses, C_0 should remain constant in Eq. (7). The eddy current effect in all samples has the same trend.

Based on Fig. 13c, the minimization of the reflection coefficient is related to the attenuation of wave amplitude at the time of transmission through the absorbent medium. In other words, the higher the attenuation coefficient, the greater the absorption will be. According to the mentioned diagram, the attenuation coefficient of the EM waves has diminished with an increase in the amount of barium ferrite nanoparticles. In Fig. 13d, the impedance of the samples has had the same trend, where the minimum value is related to GO aerogel and the maximum to the barium ferrite nanoparticles.

According to Fig. 14, it is observed that in most samples, the most internal impedance reaches one in a region of the fre-

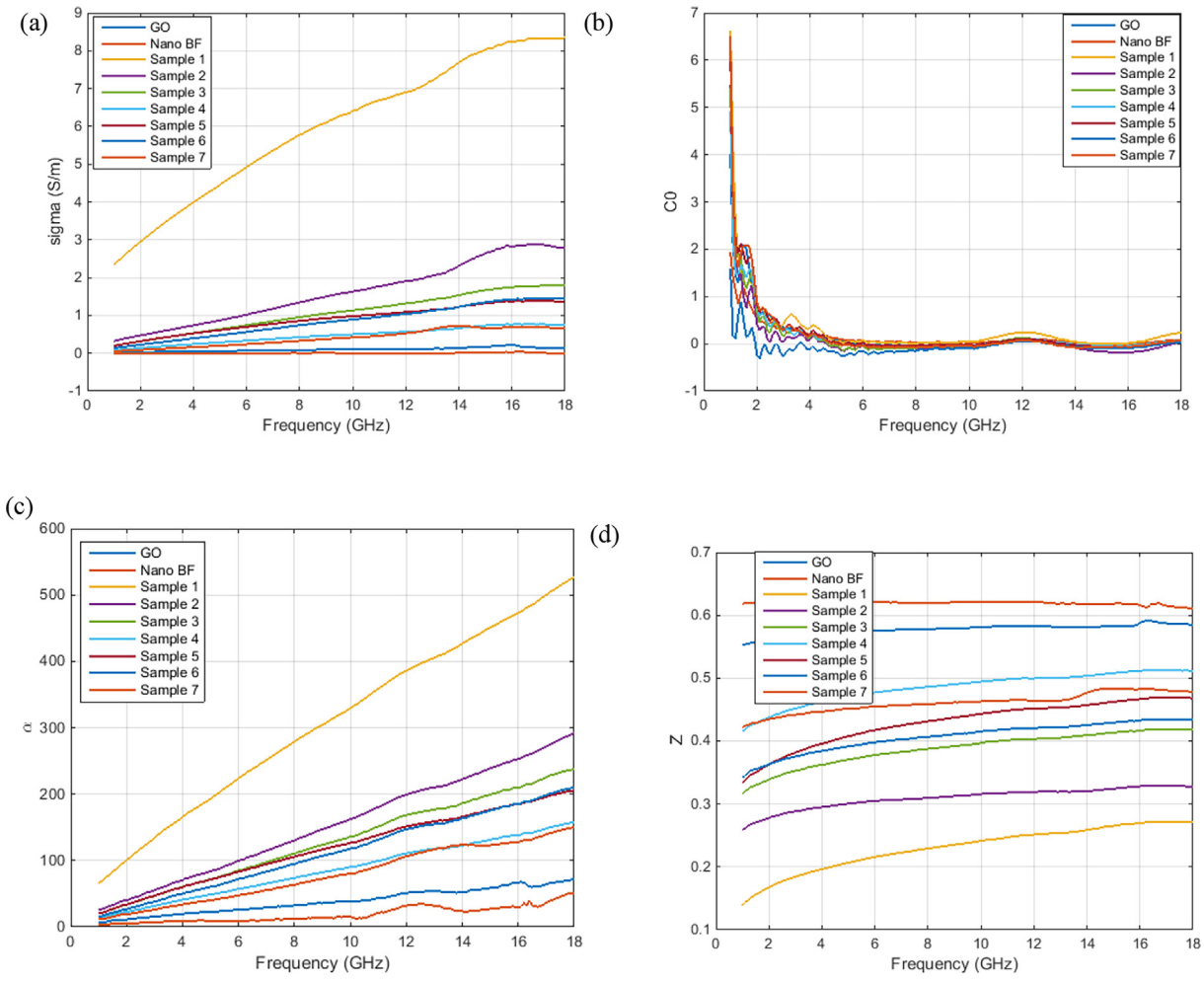

Fig. 13 A) conductivity, b) eddy current effect, c) attenuation coefficient and, d) impedance. go and sample 1 is graphene oxide nanopowders and graphene oxide aerogel.

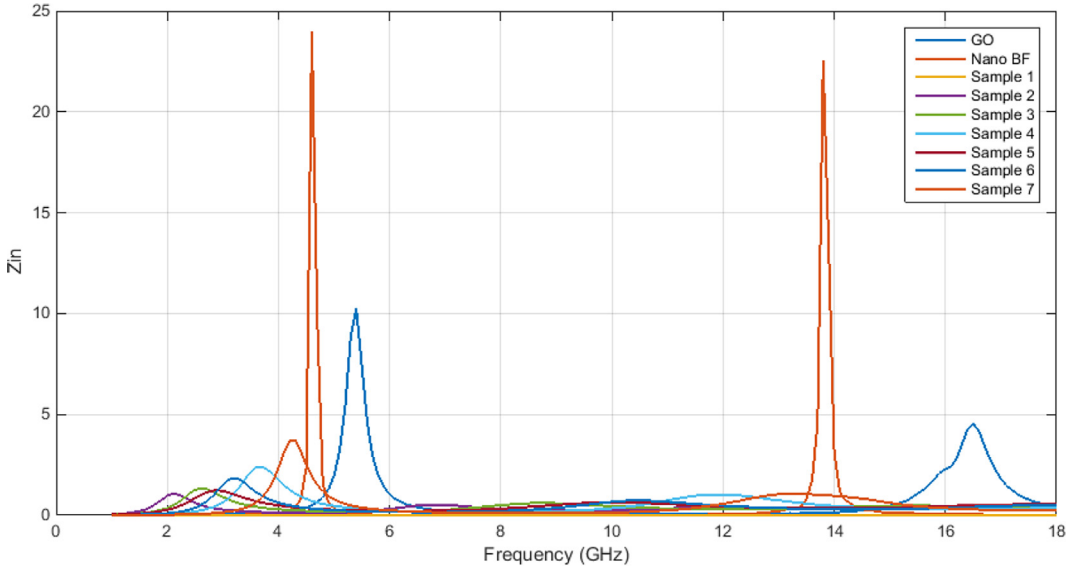

Fig. 14 Internal impedance of the samples with varying thicknesses.

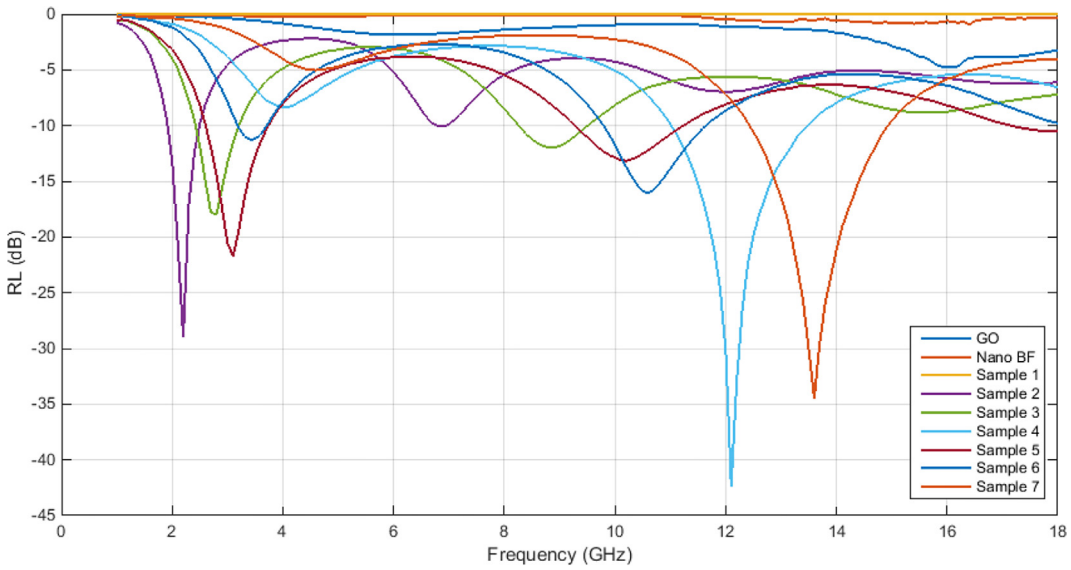

Fig. 15 RL curve of all samples with varying thicknesses.

quency range 0–18 GHz. If the internal impedance is equal to one, the impedance matching has occurred for the samples. When we have impedance matching, absorption of electromagnetic waves occurs with a high content.

The Em wave absorptivity in an absorbent is usually expressed through the reflection loss (RL) characteristic. At this stage, after examining the samples regarding the absorption of electromagnetic waves and all effective mechanisms, including magnetic losses, dielectric losses, an increase of electric conductivity, and impedance matching for every single sample, their RLs are shown in Table 4. Also, Fig. 15 has drawn the RL curve for all samples.

GO, barium ferrite nanoparticles, and GO aerogel do not have much RL value since within the frequency range 0–19 GHz, dielectric losses in GO and GO aerogel alone cannot be a factor for electromagnetic wave absorption. These conditions also apply to barium ferrite nanoparticles by having magnetic losses alone. Nevertheless, barium ferrite nanoparticles at higher frequencies can be absorbent of electromagnetic waves, and for this absorption by barium ferrite nanoparticles at X-band, either some elements should be doped in barium ferrite.

The 3GO/BF, 2GO/BF, and 3GO/2BF samples have three RL values above 10 dB at a thickness of 1–5 mm. The high saturation magnetization of the samples, as well as the high weight percentage of the barium ferrite nanoparticles compared to the GO sample, can explain the three RL peaks.

By investigating the RL curves of all samples, the best RL with −43 dB has occurred at a frequency of 12.1 GHz with a frequency range of 11–13.4 GHz at a thickness of 4 mm related to the 3GO/2BF sample. As shown in Table 4, 3GO/2BF aerogel composite show less coercivity than other samples due to the good separation of BF nanoparticles by GO nanosheets. The GO aerogel nanocomposite containing 40 wt% barium ferrite nanoparticles with a thickness of 4 can be used as an absorbent of electromagnetic waves. Other absorption properties of the electromagnetic waves of the samples are presented in Table 5.

Comparing the results of the present research with other studies (Table 6), it is seen that the best RL value obtained in this research is −43 dB as bicomponent aerogel; considering the bicomponent nature of the final product, it has had suitable RL compared to other aerogels with three components (Zhao et al., 2017; Zhang et al., 2018; Gupta et al., 2019; Feng

Table 5 Absorption properties of the electromagnetic waves of the samples.

	First reflection loss (dB)	First reflection loss absorption range (GHz)	Second reflection loss (dB)	Second reflection loss absorption range (GHz)	Third reflection loss (dB)	Third reflection loss absorption range (GHz)	Thickness (mm)
GO sample	−4.9	–	–	–			8
BF sample	−1.5	–	–	–			10
GA sample	−7.8	–	–	–			9
3GO/BF sample	−29	1.9–2.6	−10	6.8–7	−18	14.2–18	5
2GO/BF sample	−18	2.6–3.2	−12	8.4–9.6			5
3GO/2BF sample	−43	11.0–13.4	–	–			4
GO/BF sample	−22	2.6–3.8	−13	9.2–11.2			5
2GO/3BF sample	−16	9.8–11.6	−11.4	3.1–3.8			4.45
GO/2BF sample	−35	12.4–15	–	–			3.85

Table 6 Comparison with other studies.

Sample	Reflection loss (dB)	Bandwidth (GHz)	Thickness (mm)	Bulk density (mg/cm^3)	Ref.
ACNT/RGO/BF	−19.03	3.32	2		(Zhao et al., 2017)
RGO/PPy nanotube/Fe_3O_4	−49.2	3.32	3		(Zhang et al., 2018)
CoNi/N-doped graphene	−22	–	2	–	(Feng et al., 2016)
$CoFe_2O_4$/N-RGO aerogels	−60.4	6.48	2.1	–	(Wang et al., 2020)
Fe_3O_4/Fe/RGO	−23.9	3.9	4	–	(Ding et al., 2016)
$Ni_{0.8}Zn_{0.2}Ce_{0.06}Fe_{1.94}O_4$/GNS	−37.4	4	3	–	(Wang et al., 2013)
rGO/Ni	−39.03	4.3	2		(Zhang et al., 2016)
RGO	−25.6	4.8	4	–	(Xu et al., 2018)
Graphene foam	−34	14.3 (3.7–18 GHz)	10	–	(Zhang et al., 2014)
rGO/MWCNTs/Fe_3O_4	−33	3.24	3		(Zhang et al., 2016)
Graphene oxide aerogel	−30.53	4.1	1.5	7.6	(Wang et al., 2015)
N-doped graphene foams	−53.9	4.56	3.5	16.6	(Liu et al., 2019)
3GO/2BF	−43	2.4	4	8.4	This work
GO/2BF	−35	2.6	3.85	9.3	This work

et al., 2016; Wang et al., 2020; Ding et al., 2016; Wang et al., 2013; Zhang et al., 2016; Xu et al., 2018; Zhang et al., 2014; Zhang et al., 2016; Huang et al., 2018; Gordani et al., 2022; Wang et al., 2015; Liu et al., 2019). The bulk density of 3GO/2BF aerogels (Table 6) was 8.4 mg/cm^3, which was lower than the 3 components of EM wave aerogels (∼10–14 mg/cm^3) (Zhao et al., 2017; Zhang et al., 2018; Zhang et al., 2016; Zhang et al., 2016).

Due to the high specific surface area of graphene oxide nanosheets and its good wettability, their loading capacity for metal oxide nanoparticles such as barium ferrite is high. However, very large amounts of magnetic nanoparticles may increase the magnetic and dielectric parameters too much and decrease the impedance matching with the free space. Therefore, different amounts of different concentrations of barium ferrite nanoparticles (from 25 wt% to 67 wt%) were used in this research (see loading ratio in Table 2). Results show that the sample with loading 40% BF nanoparticle on GO nanosheets show the highest reflection loss value (RL = −43 dB).

4. Conclusion

Using the coprecipitation method, barium ferrite nanoparticles with hexagonal sheet-like morphology were synthesized. Then, graphene oxide aerogel/ barium ferrite nanoparticles nanocomposite was synthesized with the hydrothermal method. The electromagnetic properties and absorption of electromagnetic waves of these nanocomposites were investigated, with the following results obtained:

- By examining the XRD patterns, it was found that the synthesized barium ferrite nanoparticles were accompanied by iron oxide impurity due to synthesis conditions, including stoichiometric ratio, low barium reactivity, calcination temperature, etc. This negatively affected the magnetic behavior as well as the absorption properties of the electromagnetic waves.
- The results of FTIR spectroscopy confirmed the presence of vibrational bonds related to GO nanosheets and barium ferrite nanoparticles in all nanocomposites.
- By examining the morphology of the synthesized nanocomposites, the GO planes got detached from each other and had a 3D structure, while the barium ferrite nanoparticles were distributed onto the planes.
- After exploring the magnetic properties of the nanocomposites, it was found that having high magnetization does not necessarily justify the high absorptivity of electromagnetic waves. But the GO/BF aerogel with less coercivity (3GO/2BF) shows the highest RL value due to the good separation of BF nanoparticles by GO nanosheets.
- By testing the RL value of the samples within the frequency range 1–18 GHz, the 3GO/BF, 2GO/BF, and 3GO/2BF samples had two RL peaks, while the GO/BF, 2GO/3BF, and GO/2BF samples had three RL peaks above 10 dB at thicknesses of 1–5 mm.
- The results of measuring the absorption properties of the electromagnetic waves indicated that the maximum RL value of 43 dB within the frequency range 11–13.4 GHz with a thickness of 4 mm was related to 3GO/2BF sample.

CRediT authorship contribution statement

Reza Ghorbanpour Ghartavool: Conceptualization, Data curation, Funding acquisition, Investigation, Methodology, Project administration. **Gholam Reza Gordani:** Conceptualization, Data curation, Funding acquisition, Investigation, Methodology, Project administration. **Mohammad Reza Loghman Estarki:** Conceptualization, Data curation, Funding acquisition, Investigation, Methodology, Project administration. **Majid Tavoosi:** Conceptualization, Data curation, Funding acquisition, Investigation, Methodology, Project administration. **Mehdi Mazaheri Forushani:** Conceptualization, Data curation, Funding acquisition, Investigation, Methodology, Project administration. **Esmail Kiani:** Conceptualization, Data curation, Funding acquisition, Investigation, Methodology, Project administration.

Declaration of Competing Interest

The authors declare that they have no known competing financial interests or personal relationships that could have appeared to influence the work reported in this paper.

Appendix A. Supplementary material

Supplementary data to this article can be found online at https://doi.org/10.1016/j.arabjc.2023.105099.

References

Ain, Q.T., Haq, S.H., Alshammari, A., Al-Mutlaq, M.A., Anjum, M. N., 2019. The systemic effect of PEG-nGO-induced oxidative stress in vivo in a rodent model. Beilstein J. Nanotechnol. 10 (1), 901–911.

Anand, S., Pauline, S., Joseph Prabagar, C., 2020. Zr doped Barium hexaferrite nanoplatelets and RGO fillers embedded Polyvinylidenefluoride composite films for electromagnetic interference shielding applications. Polym. Test. 86, 106504.

Bokov, D., Turki Jalil, A., Chupradit, S., Suksatan, W., Javed Ansari, M., Shewael, I.H., Kianfar, E., 2021. Nanomaterial by sol-gel method: synthesis and application. Adv. Mat. Sci. Engin. 2021, 1–21.

Boruah, P.K., Sharma, B., Karbhal, I., Shelke, M.V., Das, M.R., 2017. Ammonia-modified graphene sheets decorated with magnetic Fe_3O_4 nanoparticles for the photocatalytic and photo-Fenton degradation of phenolic compounds under sunlight irradiation. J. Hazard. Mater. 325, 90–100.

Budi, H.S., Davidyants, A., Rudiansyah, M., Ansari, M.J., Suksatan, W., Sultan, M.Q., Kazemnejadi, M., 2022. Alendronate reinforced polycaprolactone-gelatin-graphene oxide: A promising nanofibrous scaffolds with controlled drug release. Mat. Today Commun. 32, 104108.

Cheng, Y., Zhao, H., Lv, H., Shi, T., Ji, G., Hou, Y., 2020. Lightweight and flexible cotton aerogel composites for electromagnetic absorption and shielding applications. Adv. Electron. Mater. 6 (1), 1900796.

Ding, Y., Zhang, L., Liao, Q., Zhang, G., Liu, S., Zhang, Y., 2016. Electromagnetic wave absorption in reduced graphene oxide functionalized with Fe_3O_4/Fe nanorings. Nano Res. 9, 2018–2025.

Du, S., Xie, H., Yin, J., Sun, Y., Wang, Q., Liu, H., Qi, W., et al, 2023. Giant hot electron thermalization via stacking of graphene layers. Carbon 203, 835–841.

Du, S., Xie, H., Yin, J., Fang, T., Zhang, S., Sun, Y., Cai, C., et al, 2023. Competition pathways of energy relaxation of hot electrons through coupling with optical, surface, and acoustic phonons. J. Phys. Chem. C.

Ellwood, W.B., Legg, V.E., 1937. Study of magnetic losses at low flux densities in permalloy sheet. Bell Syst. Tech. J. 16 (2), 212–227.

Feher, L.E., 2009. Energy Efficient Microwave Systems: Materials Processing Technologies for Avionic, Mobility and Environmental Applications. Springer Science & Business Media.

Feng, J., Fangzhao, P.u., Li, Z., Li, X., Xiaoyun, H.u., Bai, J., 2016. Interfacial interactions and synergistic effect of CoNi nanocrystals and nitrogen-doped graphene in a composite microwave absorber. Carbon 104, 214–225.

Feng, Y., Zhang, B.o., Liu, Y., Niu, Z., Fan, Y., Chen, X., 2022. A D-band manifold triplexer with high isolation utilizing novel waveguide dual-mode filters. IEEE Trans. Terahertz Sci. Technol. 12 (6), 678–681.

Feng, W.J., Zhao, X., Zheng, W.Q., Gang, J.T., Cao, Y., Yang, H.a., 2017. Microwave absorption properties of $BaFe_{12}O_{19}$ prepared in different temperatures with polyaniline nanocomposites. In: Advanced Materials Research, vol. 1142. Trans Tech Publications Ltd, pp. 211–215.

Forushani, M.M., Gordani, G., Ghasemi, A., Estarki, M.R.L., Torkian, S., Jamali, H., Tavoosi, M., Kiani, E., 2023a. Effect of multi-wall carbon nanotubes/strontium ferrite nanoparticles on the microstructure, phase, magnetic and electromagnetic behavior of carbon aerogel composites. J. Mater. Res. Technol. 23, 3424–3440.

Forushani, M.M., Gordani, G., Ghasemi, A., Loghman Estarki, M. R., Torkian, S., Jamali, H., Tavoosi, M., Kiani, E., 2023b. Effect of multi-wall carbon nanotubes/strontium ferrite nanoparticles on the microstructure, phase, magnetic and electromagnetic behavior of carbon aerogel composites. J. Mater. Res. Technol. 23, 3424–3440.

Fu, Z.H., Yang, B.J., Shan, M.L., Li, T., Zhu, Z.Y., Ma, C.P., Gao, W., 2020. Hydrogen embrittlement behavior of SUS301L-MT stainless steel laser-arc hybrid welded joint localized zones. Corros. Sci. 164, 108337.

Ghasemvand, M., Behjat, B., Ebrahimi, S., 2023. Experimental investigation of the effects of adhesive defects on the strength and creep behavior of single-lap adhesive joints at various temperatures. J.Adhes. 99 (7), 1227–1243.

Ghzaiel, T.B., Dhaoui, W., Pasko, A., Mazaleyrat, F., 2016. Optimization of multiroute synthesis for polyaniline-barium ferrite composites. Mater. Chem. Phys. 179, 42–54.

Gonçalves, A.H.A., Siciliano, P.H.C., Alves, O.C., Cesar, D.V., Henriques, C.A., Gaspar, A.B., 2020. Synthesis of a magnetic Fe_3O_4/RGO composite for the rapid photo-Fenton discoloration of indigo carmine dye. Top. Catal. 63, 1017–1029.

Gong, Y., Li, D., Qiang, F.u., Pan, C., 2015. Influence of graphene microstructures on electrochemical performance for supercapacitors. Prog. Nat. Sci.: Mater. Int. 25 (5), 379–385.

Gordani, G.R., Estarki, M.R.L., Kiani, E., Torkian, S., 2022. The effects of strontium ferrite micro-and nanoparticles on the microstructure, phase, magnetic properties, and electromagnetic waves absorption of graphene oxide-$SrFe_{12}O_{19}$-SiC aerogel nanocomposite. J. Magn. Magn. Mater. 545, 168667.

Guo, K., Gou, G., Lv, H., Shan, M., 2022. Jointing of CFRP/5083 aluminum alloy by induction brazing: processing, connecting mechanism, and fatigue performance. Coatings 12 (10), 1559.

Gupta, S., Sharma, S.K., Pradhan, D., Tai, N.-H., 2019. Ultra-light 3D reduced graphene oxide aerogels decorated with cobalt ferrite and zinc oxide perform excellent electromagnetic interference shielding effectiveness. Compos. A Appl. Sci. Manuf. 123, 232–241.

Hanson, R.K., Mitchell Spearrin, R., Goldenstein, C.S., 2016. In: Spectroscopy and Optical Diagnostics for Gases, Vol. 1. Springer, Berlin.

He, Y., Zhang, L.i., Tong, M.S., 2023. Microwave imaging of 3D dielectric-magnetic penetrable objects based on integral equation method. IEEE Trans. Antennas Propag.

He, F., Zhao, W., Cao, L., Liu, Z., Sun, L., Zhang, Z., Zhang, H., Qi, T., 2023. The ordered mesoporous barium ferrite compounded with nitrogen-doped reduced graphene oxide for microwave absorption materials. Small, 2205644.

Huang, Z., Chen, H., Huang, Y., Ge, Z., Zhou, Y., Yang, Y., Xiao, P., et al, 2018. Ultra-broadband wide-angle terahertz absorption properties of 3D graphene foam. Adv. Funct. Mater. 28, (2) 1704363.

Huang, X., Gaoyuan, Y.u., Zhang, Y., Zhang, M., Shao, G., 2021. Design of cellular structure of graphene aerogels for electromagnetic wave absorption. Chem. Eng. J. 426, 131894.

Jalil, T.A., Emad Al Qurabiy, H., Hussain Dilfy, S., Oudah Meza, S., Aravindhan, S., M Kadhim, M., M Aljeboree, A., 2021. CuO/ZrO2 nanocomposites: facile synthesis, characterization and photocatalytic degradation of tetracycline antibiotic. J. Nanostruct. 11 (2), 333–346.

Jasim, S.A., Hadi, J.M., Opulencia, M.J.C., Karim, Y.S., Mahdi, A.B., Kadhim, M.M. ... Falih, K.T., 2022. MXene/metal and polymer nanocomposites: preparation, properties, and applications. J. Alloys Compds. 917, 165404.

Jia, H., Kong, Q.-Q., Yang, X., Xie, L.-J., Sun, G.-H., Liang, L.-L., Chen, J.-P., Liu, D., Guo, Q.-G., Chen, C.-M., 2021. Dual-functional graphene/carbon nanotubes thick film: Bidirectional thermal dissipation and electromagnetic shielding. Carbon 171, 329–340.

Jiao, X., Qiu, Y., Zhang, L., Zhang, X., 2017. Comparison of the characteristic properties of reduced graphene oxides synthesized from natural graphites with different graphitization degrees. RSC Adv. 7 (82), 52337–52344.

Khorshidi, H., Zhang, C., Najafi, E., Ghasemi, M., 2022. Fresh, mechanical and microstructural properties of alkali-activated composites incorporating nanomaterials: A comprehensive review. J. Clean. Prod. 135390.

Kim, H.-K., Aravindan, V., Roh, M.H.-K., Lee, K., Jung, M.-H., Madhavi, S., Chul Roh, K., Kim, K.B., 2017. Exploring high-energy Li-I (r) on batteries and capacitors with conversion-type Fe_3O_4-rGO as the negative electrode. ChemElectroChem 4 (10), 2626–2633.

Kumar, A., Sadanandhan, A.M., Jain, S.L., 2019. Silver doped reduced graphene oxide as a promising plasmonic photocatalyst for oxidative coupling of benzylamines under visible light irradiation. New J. Chem. 43 (23), 9116–9122.

Liu, B., Peng, Y., Zuanming Jin, X.W., Hongyu, G.u., Wei, D., Zhu, Y., Zhuang, S., 2023. Terahertz ultrasensitive biosensor based on wide-area and intense light-matter interaction supported by QBIC. Chem. Eng. J. 462, 142347.

Liu, P., Zhang, Y., Yan, J., Huang, Y., Xia, L., Guang, Z., 2019. Synthesis of lightweight N-doped graphene foams with open reticular structure for high-efficiency electromagnetic wave absorption. Chem. Eng. J. 368, 285–298.

Magisetty, R.P., Shukla, A., Kandasubramanian, B., 2018. Magnetodielectric microwave radiation absorbent materials and their polymer composites. J. Electron. Mater. 47 (11), 6335–6365.

Majcher, K., Musiał, M., Pakos, W., Różański, A., Sobótka, M., Trapko, T., 2020. Methods of protecting buildings against HPM radiation—A review of materials absorbing the energy of electromagnetic waves. Materials 13 (23), 5509.

Marras, S.I., Kladi, K.P., Tsivintzelis, I., Zuburtikudis, I., Panayiotou, C., 2008. Biodegradable polymer nanocomposites: The role of nanoclays on the thermomechanical characteristics and the electrospun fibrous structure. Acta Biomater. 4 (3), 756–765.

Mathews, S.A., Rajan Babu, D., 2021. Analysis of the role of M-type hexaferrite-based materials in electromagnetic interference shielding. Curr. Appl Phys. 29, 39–53.

Mazaheri Forushani, M., Reza Gordani, G., Ghasemi, A., Loghman Estarki, M.R., Torkian, S., Jamali, H., Tavoosi, M., Kiani, E., 2023. Lightweight cellulose/MWCNT/$SrFe_{12}O_{19}$ aerogel composites: microstructure, density, mechanical properties, and electromagnetic behavior. Cellulose, 1–23.

Nanni, F., Valentini, M., 2011. Electromagnetic properties of polymer–carbon nanotube composites. In: Polymer-Carbon Nanotube Composites. Woodhead Publishing, pp. 329–346.

Ngafwan, N., Rasyid, H., Abood, E.S., Abdelbasset, W.K., Al-Shawi, S. G., Bokov, D., Jalil, A.T., 2021. Study on novel fluorescent carbon nanomaterials in food analysis. Food Sci. Technol. 42, e37821.

Pavithra, A., Ajay Rakkesh, R., Durgalakshmi, D., Balakumar, S., 2017. Room temperature detection of hydrogen gas using graphene-based conductometric gas sensor. J. Nanosci. Nanotechnol. 17 (5), 3449–3453.

Sharma, N., Sharma, V., Jain, Y., Kumari, M., Gupta, R., Sharma, S. K., Sachdev, K., 2017. Synthesis and characterization of graphene oxide (GO) and reduced graphene oxide (rGO) for gas sensing application. In: Macromol. Symp. vol. 376, 2017, p. 1700006.

Radjehi, L., Aissani, L., Djelloul, A., Saoudi, A., Lamri, S., Nomenyo, K., Sanchette, F., 2023. Air and Vacuum Annealing Effect on the Highly Conducting and Transparent Properties of the Undoped Zinc Oxide Thin Films Prepared by DC Magnetron Sputter. Metallurgical Mat. Eng. 29 (1), 37–51.

Raya, I., Chupradit, S., Kadhim, M.M., Mahmoud, M.Z., Jalil, A.T., Surendar, A., Bochvar, A.N., 2022. Role of compositional changes on thermal, magnetic, and mechanical properties of Fe-PC-based amorphous alloys. Chine. Physics B 31, (1) 016401.

Sadeghi, M., Yousefi Siavoshani, A., Bazargani, M., Jalil, A.T., Ramezani, M., Poor Heravi, M.R., 2022. Dichlorosilane adsorption on the Al, Ga, and Zn-doped fullerenes. Monatshefte für Chemie-Chemical Monthly 153 (5–6), 427–434.

Salahdin, O.D., Sayadi, H., Solanki, R., Parra, R.M.R., Al-Thamir, M., Jalil, A.T., Kianfar, E., 2022. Graphene and carbon structures and nanomaterials for energy storage. Appli. Phys. A 128 (8), 703.

Shen, W., Ren, B., Cai, K., Song, Y.-F., Wang, W., 2019. Synthesis of nonstoichiometric $Co_{0.8}Fe_{2.2}O_4$/reduced graphene oxide (rGO) nanocomposites and their excellent electromagnetic wave absorption property. J. Alloy. Compd. 774, 997–1008.

Shi, Y., Guo, Z., Zhu, D., Pan, J., Lu, S., 2023. Isothermal reduction kinetics and microstructure evolution of various vanadium titanomagnetite pellets in direct reduction. J. Alloys Compods. 953, 170126.

Sivaraman, R., Patra, I., Opulencia, M.J.C., Sagban, R., Sharma, H., Jalil, A.T., Ebadi, A.G., 2022. Evaluating the potential of graphene-like boron nitride as a promising cathode for Mg-ion batteries. J. Electroanal. Chem. 917, 116413.

Song, Z., Shao, X., Wei, W.u., Liu, Z., Yang, M., Liu, M., Wang, H., 2023. Structures and stabilities of carbon chain clusters influenced by atomic antimony. Molecules 28 (3), 1358.

Su, Z., Meng, J., Su, Y., 2023. Application of SiO_2 nanocomposite ferroelectric material in preparation of trampoline net for physical exercise. Adv. Nano Res. 14, 355–362. https://doi.org/10.12989/anr.2023.14.4.355.

Suanto, P., Usman, A.P., Saggaff, A., Ismail, M., Khalid, N.H.A., 2022. The characterization of nanocellulose with various durations and NaOH concentration. Int. J. Innovative Res. Scientific Studies 5 (1), 18–29.

Sun, N. et al, 2023. Breakup and coalescence mechanism of high-stability bubbles reinforced by dispersed particle gel particles in the pore-throat micromodel. Geoenergy Sci. Eng. 223, 211513.

Sun, Z., Fang, S., Yun Hang, H.u., 2020. 3D graphene materials: from understanding to design and synthesis control. Chem. Rev. 120 (18), 10336–10453.

Vinay, K., Shivakumar, K., Ravikiran, Y.T., Revanasiddappa, M., Raghavendra, S.C., 2018. Synthesis, characterization, ac conductivity and humidity sensing behaviour of polyaniline/$BaFe_{12}O_{19}$ composite embedded with silver particles. In: 2018 Advances in Science and Engineering Technology International Conferences (ASET). IEEE, pp. 1–5.

Wang, Y. et al, 2015. Hybrid of MoS_2 and reduced graphene oxide: a lightweight and broadband electromagnetic wave absorber. ACS Appl. Mater. Interfaces 7 (47), 26226–26234.

Wang, Z., Chen, C., Liu, H., Hrynshpan, D., Savitskaya, T., Chen, J., Chen, J., 2020. Enhanced denitrification performance of Alcaligenes sp. TB by Pd stimulating to produce membrane adaptation mechanism coupled with nanoscale zero-valent iron. Sci. Total Environ. 708, 135063.

Wang, Z., Dai, L., Yao, J., Guo, T., Hrynsphan, D., Tatsiana, S., Chen, J., 2021. Enhanced adsorption and reduction performance of nitrate by Fe–Pd–Fe_3O_4 embedded multi-walled carbon nanotubes. Chemosphere 281, 130718.

Wang, C., Ding, Y., Yuan, Y., He, X., Wu, S., Hu, S., Zou, M., et al, 2015. Graphene aerogel composites derived from recycled cigarette filters for electromagnetic wave absorption. J. Mater. Chem. C 3 (45), 11893–11901.

Wang, Y., Huang, Y., Wang, Q., Zong, M., 2013. Preparation and electromagnetic properties of graphene-supported $Ni_{0.8}Zn_{0.2}Ce_{0.06}Fe_{1.94}O_4$ nanocomposite. Powder Technol. 249, 304–308.

Wang, X., Yukai, L.u., Zhu, T., Chang, S., Wang, W., 2020. $CoFe_2O_4$/N-doped reduced graphene oxide aerogels for high-performance microwave absorption. Chem. Eng. J. 388, 124317.

Xia, Y., Gao, W., Gao, C., 2022. A review on graphene-based electromagnetic functional materials: electromagnetic wave shielding and absorption. Adv. Funct. Mater. 32 (42), 2204591.

Xu, K.-D., Guo, Y.-J., Liu, Y., Deng, X., Chen, Q., Ma, Z., 2021. 60-GHz compact dual-mode on-chip bandpass filter using GaAs technology. IEEE Electron Device Lett. 42 (8), 1120–1123.

Xu, K.-D., Liu, Y., 2023. Millimeter-wave on-chip bandpass filter using complementary-broadside-coupled structure. IEEE Trans. Circ. Syst. II: Express Brief.

Xu, W., Wang, G.-S., Yin, P.-G., 2018. Designed fabrication of reduced graphene oxides/Ni hybrids for effective electromagnetic absorption and shielding. Carbon 139, 759–767.

Yang, Q., Liu, L., Hui, D., Chipara, M., 2016. Microstructure, electrical conductivity and microwave absorption properties of γ-FeNi decorated carbon nanotube composites. Compos. B Eng. 87, 256–262.

Yi, J., Choe, G., Park, J., Lee, J.Y., 2020. Graphene oxide-incorporated hydrogels for biomedical applications. Polym. J. 52 (8), 823–837.

Yusof, A.A., 2004. The development of microwave absorber from oil palm shell carbon. Universiti Teknologi Malaysia. PhD diss..

Zhang, S., Cao, Q., 2012. Electromagnetic and microwave absorption performance of some transition metal doped $La_{0.7}Sr_{0.3}Mn_{1-x}TM_xO_{3\pm\delta}$ (TM = Fe, Co or Ni). Mater. Sci. Eng. B 177 (9), 678–684.

Zhang, C., Chen, Y., Li, H.a., Tian, R., Liu, H., 2018. Facile fabrication of three-dimensional lightweight RGO/PPy nanotube/Fe_3O_4 aerogel with excellent electromagnetic wave absorption properties. ACS Omega 3 (5), 5735–5743.

Zhang, H., Hong, M., Chen, P., Xie, A., Shen, Y.H., 2016. 3D and ternary rGO/MCNTs/Fe_3O_4 composite hydrogels: synthesis, characterization and their electromagnetic wave absorption properties. J. Alloy. Compds. 665, 381–387.

Zhang, Y.i., Huang, Y.i., Chen, H., Huang, Z., Yang, Y., Xiao, P., Zhou, Y., Chen, Y., 2016. Composition and structure control of ultralight graphene foam for high-performance microwave absorption. Carbon 105, 438–447.

Zhang, X., Tang, Y., Zhang, F., Lee, C.-S., 2016. A novel aluminum–graphite dual-ion battery. Adv. Energy Mater. 6 (11), 1502588.

Zhang, X.-J., Wang, G.-S., Cao, W.-Q., Wei, Y.-Z., Cao, M.-S., Guo, L., 2014. Fabrication of multi-functional PVDF/RGO composites via a simple thermal reduction process and their enhanced electromagnetic wave absorption and dielectric properties. RSC Adv. 4 (38), 19594–19601.

Zhang, J., Wang, X., Zhou, L., Liu, G., Adroja, D.T., da Silva, I., Demmel, F., et al, 2022. A ferrotoroidic candidate with well-separated spin chains. Adv. Mater. 34 (12), 2106728.

Zhang, H., Xiao, Y., Xu, Z., Yang, M., Zhang, L., Yin, L., Chai, S., Wang, G., Zhang, L., Cai, X., 2022. Effects of Ni-decorated reduced graphene oxide nanosheets on the microstructural evolution and mechanical properties of $Sn_{-3.0}$ $Ag_{-0.5}$ Cu composite solders. Intermetallics 150.

Zhang, Q., Zhang, F., Medarametla, S.P., Li, H., Zhou, C., Lin, D., 2016. 3D printing of graphene aerogels. Small 12 (13), 1702–1708.

Zhao, Y., 2022. Co-precipitated Ni/Mn shell coated nano Cu-rich core structure: A phase-field study. J. Mater. Res. Technol. 21, 546–560.

Zhao, T., Ji, X., Jin, W., Xiong, C., Ma, W., Wang, C., Duan, S., et al, 2017. Synthesis and electromagnetic wave absorption property of amorphous carbon nanotube networks on a 3D graphene aerogel/$BaFe_{12}O_{19}$ nanocomposite. J. Alloys Compds. 708.

Zhao, G., Li, Z., Cheng, B., Zhuang, X., Lin, T., 2023. Hierarchical porous metal organic framework aerogel for highly efficient CO_2 adsorption. Sep. Purif. Technol. 315, 123754.

Zhou, X., Jia, Z., Feng, A., Wang, X., Liu, J., Zhang, M., Cao, H., Guanglei, W., 2019. Synthesis of fish skin-derived 3D carbon foams with broadened bandwidth and excellent electromagnetic wave absorption performance. Carbon 152, 827–836.

Zhu, H., Junhao, S.u., Yang, F., Yuping, W.u., Ye, J., Huang, K., Yang, Y., 2023. Effect of lossy thin-walled cylindrical food containers on microwave heating performance. J. Food Eng. 337, 111232.